University of Basel

Master Thesis

Investigating Magnetism in Two-Dimensional CrI_3 Using Single Spin Nitrogen-Vacancy Centers in Diamond

Author: Märta Tschudin

Date: January 31, 2019

Supervised by:

Prof. Patrick Maletinsky

Abstract

In this Thesis we use single Nitrogen-Vacancy (NV) center electronic spins in diamond to investigate magnetism in atomically thin chromium triiodide (CrI_3) – a recently discovered van der Waals (vdW) magnet. A scanning probe technique with an NV center embedded in a diamond pillar is employed for quantitative, magnetic imaging. We determine the monolayer magnetization of CrI_3 to be $\sim 16\ \mu_B/\mathrm{nm}^2$, close to the theoretically expected value of $14.7\ \mu_B/\mathrm{nm}^2$. In our studies we further observe the effect of antiferromagnetic interlayer exchange coupling – in literature often referred to as the *even-odd effect* – from few-layer (≤ 9 layers) down to monolayer CrI_3. An odd number of CrI_3 layers shows a magnetization comparable to one fully polarized magnetic layer whereas the magnetization in even-layered CrI_3 vanishes. Importantly, we were able to induce switching between ferro- and antiferromagnetic interlayer ordering by structural modifications of the material. These findings imply a connection between the interlayer exchange coupling and the crystal structure of CrI_3. Our results open the way to nanoscale studies of two-dimensional magnetism in vdW magnetic materials.

Contents

Acknowledgements

First of all, I would like to thank my supervisor Patrick Maletinsky for his guidance throughout this Thesis and for all the inspiring discussions about physics. I am deeply grateful to Lucas Thiel who introduced me to his 4K magnetometry setup. I appreciated his didactical talent when imparting his knowledge a lot and I am thankful for all the tips and tricks he showed me when working in the lab. It was always fun to look for CrI_3 flakes together and thereby discovering the funniest micron sized hBN creatures (see Rorschach Appendix)!

Also, I want to thank all the members of the quantum sensing group: Thank you for all your professional help and advise in the lab and the fun sport activities from Völkerball to orienteering outside the University.

Furthermore, I am thankful to Dr. Marta De Luca from the Nanophononics lab who helped me with the room-temperature Raman measurements. Also, I would like to thank the Particles and Cosmology group of Prof. Stefan Antusch who provided me with an office space in the theory floor.

Finally, I would like to thank my friends and family for their support ♡! Thank you to Max and Johannes, my roommates and best Google-translator-game-players from the Franz-WG. Shout-out to Anja, Salome and Juri. And of course a big thank-you to Mama, Papa, my little-big brother and to my grandparents.

I gratefully acknowledge the financial support in form of the QSIT Master Internship Award.

1 Introduction

The discovery of two-dimensional van der Waals (vdW) magnets has attracted widespread interest due to their potential for a novel, atomic-scale platform with promising applications in spintronics [1, 2]. The study of magnetism in two-dimensional materials is crucial to understand spin behavior and properties in low dimensions. One of these recently discovered vdW magnets is chromium triiodide (CrI_3), which shows magnetic order down to the monolayer [3]. First experiments on CrI_3 suggest – against predictions from theory – that the material exhibits antiferromagnetic interlayer exchange coupling at low temperatures [3], which is often referred to as the *even-odd effect*: An odd number of CrI_3 layers reveals a magnetization comparable to one fully polarized magnetic layer whereas the magnetization for an even number of layers vanishes. However, to date only qualitative studies on CrI_3 exist and quantitative evidence for the even-odd effect is still lacking.

Measurement Approach

Here, we quantitatively investigate magnetism in atomically thin CrI_3 using single-spin Nitrogen -Vacancy (NV) centers for magnetic imaging. NV centers are paramagnetic defects in diamond and capable of measuring magnetic fields due to their spin dependent fluorescence [5, 6].

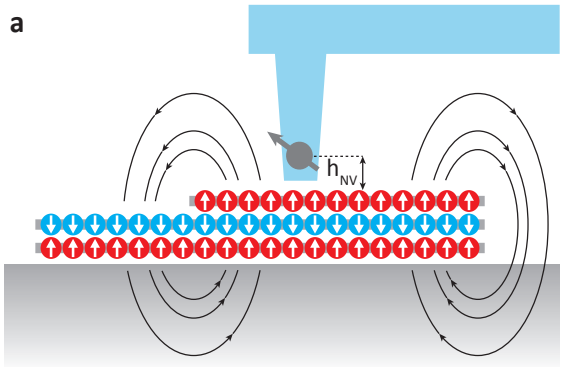

Figure 1.1: **Nitrogen-Vacancy (NV) scanning probe technique for magnetic imaging.** A single NV center at the bottom of a diamond pillar (blue) scans the sample surface to detect magnetic stray fields (black circular lines) at a height h_{NV}. We examine magnetism in the van der Waals (vdW) magnet chromium triiodide (CrI_3) (red and blue layers), which supposedly reveals antiferromagnetic interlayer coupling (indicated by white arrows) at low temperatures. Image adapted from [4] with permission from Lucas Thiel.

The NV center is a suitable tool for high precision sensing as it is a non-perturbative sensor. It operates both at room temperature and under cryogenic conditions with a spatial resolution down to the nanometer scale for a small NV-to-sample distance [5]. We employ a scanning probe approach as illustrated in Fig. 1.1, where a single NV spin (gray arrow) is embedded in the tip of a diamond pillar, which scans the sample surface and detects magnetic stray fields. Our measurements investigate the interlayer exchange coupling (antiferromagnetic versus ferromagnetic) in CrI_3 and shed light on the correlation between structural order and magnetization of the material.

Findings and Outline

Our measurements on encapsulated CrI_3 flakes at low temperatures confirm:

- Consistent with antiferromagnetic interlayer coupling, we observe a magnetization only for odd-layered CrI_3 devices, whereas zero magnetization is detected from even-layered CrI_3 samples.
- The magnetization of several CrI_3 samples with an odd number of layers (down to monolayer) was determined to be $\sim 16\ \mu_B/\mathrm{nm}^2$, comparable to the theoretically expected value of $14.7\ \mu_B/\mathrm{nm}^2$ [7].
- We observe a connection between the interlayer exchange coupling and the crystal structure of CrI_3.
- In our experiments we were able to determine the nucleation field required to induce a domain in tri-layer CrI_3 and an upper bound on the coercive field for monolayer CrI_3 was found.

The outline of this Thesis is as follows: First, we discuss the properties of the vdW magnet CrI_3 and the basic principles of NV magnetometry in Chap. 2. Second, in Chap. 3 the measurement apparatus and the studied devices are presented. Third, in Chap. 4, we discuss the measurement results on antiferromagnetic interlayer coupling in CrI_3 in Sect. 4.1. Afterwards, the correlation between stacking order and magnetization in CrI_3 is elucidated in Sect.4.2. In the last section (Sect.4.3) of Chap. 4, we discuss magnetization reversal and domains in CrI_3. Finally, we summarize our results and give an outlook in Chap. 5.

Research Context

This work was carried out in the quantum sensing lab of Prof. Patrick Maletinsky at the University of Basel. The CrI_3 project is a collaboration with the quantum electronics group of Prof. Alberto Morpurgo at the University of Geneva. The devices were fabricated in Geneva and the data presented in this Thesis were measured in Basel together with Lucas Thiel. Personally, I independently performed the measurement of the dataset shown in Fig. 4.1, the annealing tests discussed in Sect. 4.2.3, the data and analysis of Sect. 4.3 (except Fig. 4.9) and the $g^{(2)}(\tau)$ measurement (appendix A). The room-temperature Raman data from Fig. 4.7 were taken in the Nanophononics lab together with Dr. Marta De Luca. The low-temperature Raman spectra (Fig. 4.6) were recorded in Geneva. All other datasets shown in this Thesis were collected in collaboration with Lucas Thiel and a manuscript is currently under review [4].

2 Theoretical Background

A ferromagnet is defined as a material, where the spins of the magnetic moments align with respect to each other without the necessity of an external magnetic field. The magnetic order in such materials is present for temperatures below the Curie-temperature (T_c) and is caused by exchange interactions between the individual spins [8, 9]. Ferromagnetism is well known in bulk but has only recently been discovered in two-dimensional vdW structures [3]. The study of atomically thin vdW magnets requires a method for the quantitative determination of the material's magnetization. In this chapter, we first discuss the origin of magnetism in the vdW magnet CrI_3 and then cover the basic concept of NV sensing, a magnetic field measurement technique with single spins in diamond.

2.1 Van der Waals Magnet CrI_3

Two-dimensional vdW crystals are atomically thin layers of covalently bonded atoms. Weak vdW forces in between the individual layers keep a stack of two-dimensional structures together [11]. In this work we study magnetic order in the trihalide CrI_3. A trihalide is composed of a transition metal atom (A) and a halogen atom (Z) [12]:

$$AZ_3, \quad \text{in the case of } CrI_3: \ A = Cr, Z = I. \tag{2.1}$$

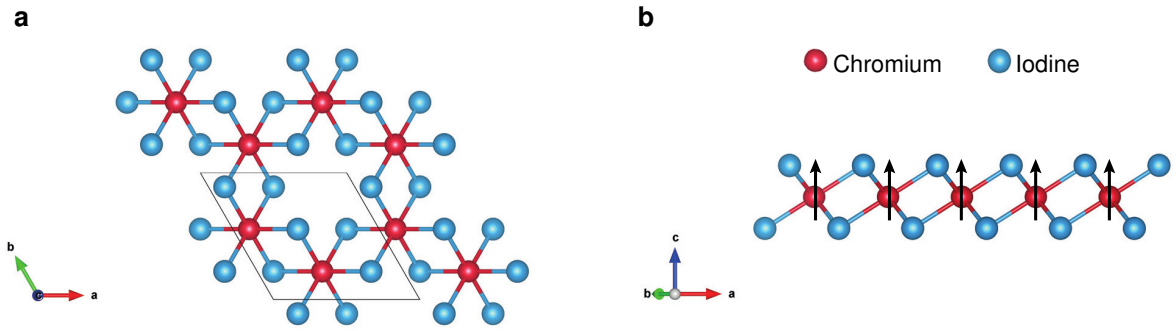

Figure 2.1: **CrI_3 structure.** **a** Chromium (Cr) atoms (red) of a single layer CrI_3 arrange in a honeycomb structure. One Cr atom is bound to six neighboring Iodine (I) atoms (blue). View along the a-b-plane. A unit cell contains two Cr atoms and six I atoms, as indicated by a black rhombus. **b** Side-view of CrI_3 showing the spin orientation (black arrows) of the magnetic moments of Cr $\sim 3\,\mu_B$. A single layer of CrI_3 was measured to be 0.7 nm in thickness [3]. The atomic structures were created with the visualization program VESTA and the crystallographic data was taken form [10].

In a single layer CrI_3 the Cr atoms form a honeycomb structure, as illustrated in Fig 2.1a. Each Cr atom is bound to six neighboring I atoms in an octahedral symmetry. A magnetic moment of 3 μ_B is attributed to each Cr atom due to the three remaining electrons in the 3d shell and similarly to bulk CrI_3, the magnetic polarization is oriented perpendicular to the atomic plane, c.f. Fig 2.1b [7]. Throughout one atomic layer the coupling of the individual spins is ferromagnetic [13].

In theory, long-range magnetic order in two-dimensional isotropic spin systems is prohibited by the Mermin-Wagner theorem [14]. However, the breaking of rotational invariance and hence the presence of anisotropy can lift this restriction and lead to magnetism in two-dimensional crystals [13]. The origin of magnetism in CrI_3 is attributed to anisotropy along the off-plane axis [13]. Super-exchange interactions between two Cr atoms separated by one I atom lead to ferromagnetic coupling in the system due to the approximately $\sim 90°$ angle between the atomic bonds [15]. The anisotropic interactions in CrI_3 result from spin-orbit coupling in the material and the correct Hamiltonian describing CrI_3 is still under debate. Lado *et al.* conclude from their density functional theory (DFT) calculations that anisotropic symmetric exchange coupling stabilizes the magnetic order [13]. While their DFT results suggest that Dzyaloshinski-Moriya (DM) interactions are negligible in CrI_3, Chen *et al.* found evidence for the presence of a DM term in the Hamiltonian with neutron scattering experiments on CrI_3 [16].

Predicted by DFT calculations and approved by experiments is the fact that CrI_3 is a semiconductor with a band gap of 1.2 eV [13]. Furthermore, it is known that in its bulk form CrI_3 is a ferromagnet with a Curie temperature of 61 K. Magneto-optical Kerr effect (MOKE) measurements by Huang *et al.* [3] suggest that the ferromagnetism persists down to monolayer CrI_3, for which a Curie temperature of 45 K was found.

Experiments and theory predict that CrI_3 arranges in two different crystal phases, which are both linked to the magnetic interlayer coupling [7, 17]. For temperatures above 220 K, CrI_3 is in the monoclinic phase, which is predicted to exhibit antiferromagnetic interlayer coupling, c.f. 2.2a [17]. Upon cooling below 220 K the material arranges in the rhombohedral phase, which is associated with ferromagnetic interlayer coupling, c.f. 2.2b. In contradiction to this, Huang *et al.* observed with MOKE indications of a layer dependent magnetic phase

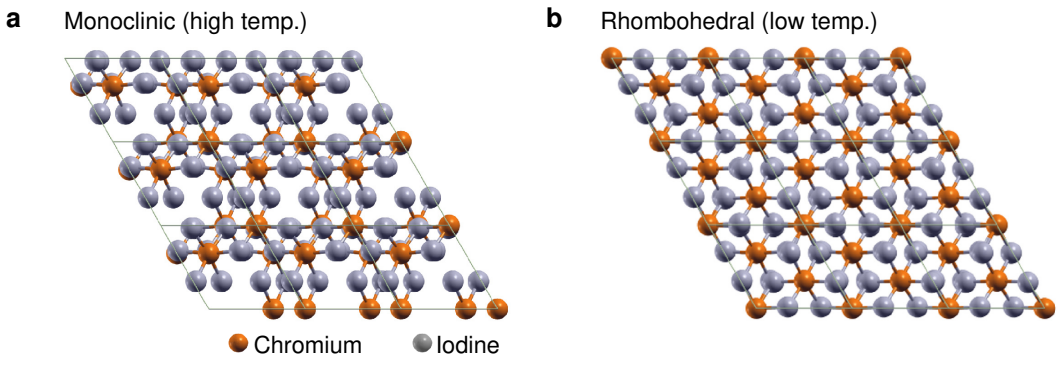

Figure 2.2: **Crystal phases of CrI_3.** **a** Monoclinic (high temperature) stacking of CrI_3 (brown atoms = Cr, grey atoms = I). **b** Rhombohedral (low temperature) stacking order. Picture adapted from [17].

in few-layer CrI_3 at low temperatures: While samples with odd numbers of CrI_3 layers show a nonzero Kerr angle, attributed to the presence of a net magnetization, even-layered devices exhibit no measurable Kerr angle, i.e. vanishing magnetization. This so called even-odd effect could be explained by antiferromagnetic interlayer coupling, where the magnetic moments of two adjacent atomic CrI_3 layers reveal opposite polarization, which leads to zero net magnetization for an even amount of layers. The existence of the even-odd effect would imply that an encapsulated stack of CrI_3 layers is coupled antiferromagnetically at $T < T_c$, instead of ferromagnetically as expected for the low-temperature phase.

One drawback of MOKE is its inability for a quantitative magnetization determination: The observed rotation of the Kerr angle differs by orders of magnitude between a monolayer sample and a tri-layer sample [3]. This is in strong contradiction to the even-odd effect based on antiferromagnetic interlayer coupling, where one would expect to measure the same signal from any odd-layered CrI_3 structure. Moreover, it has been shown that MOKE measurements can yield a non-zero magnetization for antiferromagnets [18].

To address the question whether or not the even-odd effect exists in CrI_3 a quantitative measurement method for determining the magnetization is needed. A promising candidate for non-invasive high precision quantum sensing is the NV center in diamond. In the next section we explain the fundamental principles of NV spins, their ability to sense magnetic stray fields and the analysis procedure used to determine the magnetization from the measurement data.

2.2 Magnetic Sensing based on Nitrogen-Vacancy Spins

The NV center is a paramagnetic defect in diamond whose spin can be prepared and read out optically, allowing for the detection of local magnetic fields [5, 6]. The non-perturbative nature of this solid state spin make it a suitable tool for high precision quantum sensing [19, 20].

An NV center is formed by the replacement of two carbon atoms in the diamond lattice by a Nitrogen atom and a Vacancy, c.f. Fig. 2.3a. In our magnetometry measurements we studied the negatively charged NV^-, which has an additional sixth electron in combination with the five electrons coming from the dangling bonds of three carbon atoms and the Nitrogen-Vacancy pair. In this work, we will for simplicity refer to the NV^- as the NV center.

The localized electronic states associated with the defect have a ground state spin $S = 1$ that can be initialized and read out via optical transitions. Both, ground state (GS) and excited state (ES) of the NV center have three spin sub-levels: $m_s{=}0$ and $m_s{=}\pm1$. The zero-field splitting of the GS (ES) originates from spin-spin interactions and was measured to be 2.87 GHz (1.42 GHz) [22]. A schematic of the NV level structure is shown in Fig.2.3b.

The NV spin can be excited optically with illumination of above-resonance 532 nm laser light into the ES, which has a lifetime of about $\sim$ 13 ns [23]. Spin-preserving decays to the GS occur via the emission of a 637 nm photon in the zero-phonon line (ZPL) or the emission of phonons along with photons in the phonon-sideband (PSB), which extends from $\sim$650 nm to $\sim$750 nm. The majority of the NV luminescence is coming from the PSB and only about $\sim$3 % of the emission comes from the ZPL [24, 25]. While quantum entanglement applications rely on indistinguishable photons from the ZPL, the full emission spectra is of use in NV magnetometry measurements. Essential for optimal readout and initialization are the non-spin conserving decay channels, which predominantly occur from the ES $m_s{=}\pm1$

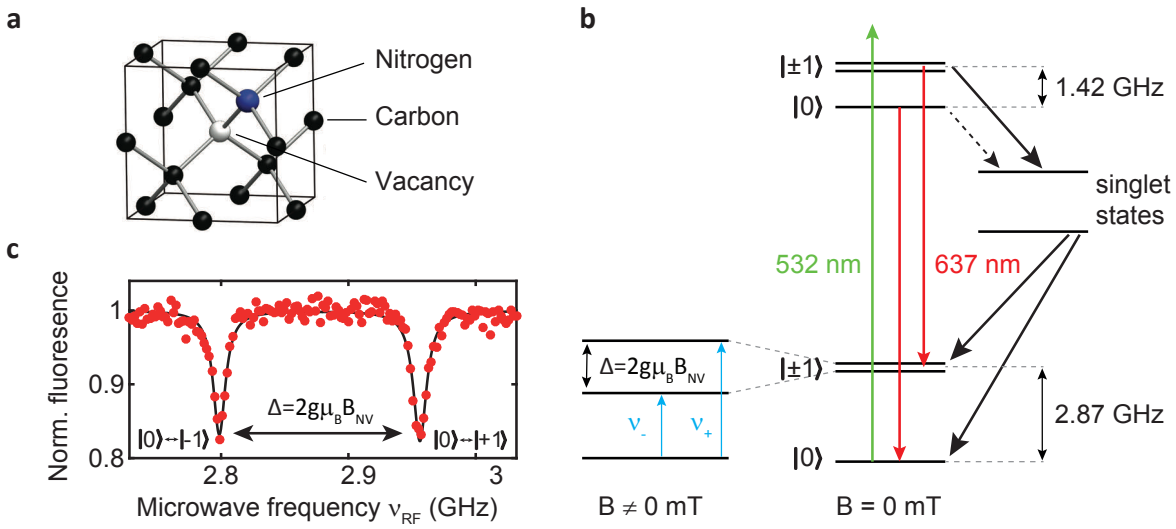

Figure 2.3: **The Nitrogen-Vacancy (NV) center in diamond.** **a** Replacing two carbon atoms (black) in the diamond lattice by a Nitrogen atom (blue) and a Vacancy (white) creates the NV center. Picture modified from [21]. **b** NV spin state level scheme: Above-resonant laser light (green arrow) can excite the GS spin triplet into the ES. Decays from the ES sub-levels occur under the emission of red fluorescence (red arrows) or via the non-radiative singlet states. In addition to the zero-field splitting of the GS (ES) 2.87 GHz (1.42 GHz), the spin sub-levels split linearly with the field strength of an applied magnetic field along the NV-axis. The transitions between the m_s=0 and m_s=±1 GS can be driven by microwaves with frequencies $\nu_{+/-}$ (blue arrows). **c** Optically-detected magnetic resonance (ODMR) measurement. The NV fluorescence is probed under continuous illumination with green laser light while the microwave driving frequency is being swept. Dips in fluorescence occur whenever the microwave frequency is in resonance with a spin transition. Image **c** is shown with permission of Lucas Thiel.

states via metastable singlet states that have longer lifetimes than the triplet ES (142 ns at 450 K, 462 ns at 4.4 K) [26]. These pathways are non-radiative and hence lead to spin-dependent fluorescence: The m_s=±1 states couple more strongly into the dark, long-lived metastable states, from where they cannot emit photons and are prevented from immediately undergoing another excitation cycle. Additionally, since these non-radiative decays are not spin-conserving and primarily take place from the ES m_s=±1 states, optical pumping into the m_s=0 GS occurs. The system can thereby be initialized into the m_s=0 GS with an 80% yield by 532 nm laser light illumination [26].

A magnetic field along the NV-axis, i.e. along the bond from the Nitrogen to the Vacancy, shifts the NV spin sub-levels due to Zeeman shifting, c.f. Fig.2.3b, left side. Microwave fields can drive the transitions between the m_s=0 and m_s=±1 GS at frequencies $\nu_{+/-}$. Illuminating the NV center with above-resonance laser light and recording its photoluminescence while varying the microwave driving frequency allows for the detection of optically-detected magnetic resonance (ODMR). Once the microwave frequency matches a spin transition from the m_s=0 to the m_s=±1 GS the system starts populating the m_s=±1 states. Upon illumination with laser light the system is then excited into the ES m_s=±1 states. From there the state can relax back to the GS via the non-radiative pathway, which leads to a reduced fluorescence. A

typical ODMR measurement is shown in Fig. 2.3c. The dips in photoluminescence occur each time the microwave frequency is on resonance with the NV spin transition from the m_s=0 to the m_s=±1 GS. The splitting Δ of the dips is proportional to B_{NV}, the magnetic field along the NV-axis [22]:

$$\Delta = 2g\mu_B \cdot B_{\mathrm{NV}}, \tag{2.2}$$

where $g\mu_B$=γ_{NV}=27.9 MHz mT^{-1} is the gyromagnetic ratio. Determining the splitting Δ is therefore a direct measurement of the local magnetic field projected onto the NV symmetry axis. Fields orthogonal to the NV symmetry axis lead to a mixing of the spin sublevels, which alters the Zeeman response [22]. However, this effect is negligible for fields studied in this work (fields smaller than 5 mT) and we can therefore assume that the NV sensor is mostly insensitive to transverse fields.

For magnetic imaging we employ a scanning probe technique, where a single NV sensor is embedded in a diamond pillar, which scans the sample surface (c.f. Fig. 1.1). ODMR spectra are acquired at multiple points in a plane above the sample. The spatial resolution is thereby limited by the NV to sample distance [20, 27], which was typically around ∼ 60 nm in our experiments (c.f. Chap. 4). Acquiring two-dimensional magnetic field maps with ODMR measurements can be very time consuming, as it usually requires an integration time of a few seconds at each point in order to achieve sufficient ODMR contrast. An alternative, faster measuring technique for obtaining magnetic contrast images is isomagnetic field (iso-field) imaging, which is illustrated in Fig. 2.4.

Figure 2.4a shows the NV GS m_s=0 to GS m_s=1 transition, which is split by the zero-field splitting and the Zeeman shift from an applied magnetic field. Instead of sweeping the microwave frequency as it is done in ODMR measurements the microwave output is set to the frequency ν_0. Simultaneously, the NV's luminescence is being recorded as the sample surface is scanned below the NV center. Whenever magnetic structures are scanned, the corresponding

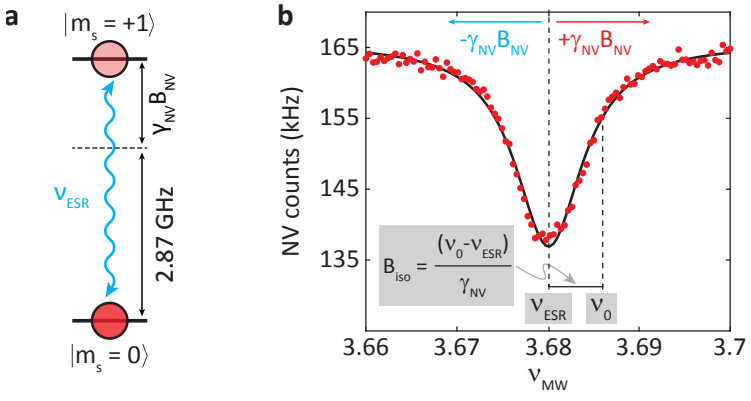

Figure 2.4: **The principle of iso-field imaging.** **a** Level scheme of the NV GS m_s=0 to m_s=1 transition, which is split by the zero-field splitting of 2.87 GHz and an applied, static magnetic field. **b** During iso-field imaging the microwave frequency is fixed at $\nu_0 = \nu_{\mathrm{ESR}} + \gamma_{\mathrm{NV}} B_{\mathrm{iso}}$ while the NV fluorescence is constantly being probed. Whenever the NV is scanned over a magnetic structure, the corresponding stray field leads to an increase or decrease in fluorescence. Maximal magnetic contrast is achieved for magnetic fields B_{iso}. Figure created by Lucas Thiel. Taken from the supplementary information of [4].

stray fields change the NV level splitting, which leads to an increase or decrease in fluorescence. Maximal contrast is observed for magnetic fields

$$B_{\text{iso}} = \frac{\nu_0 - \nu_{\text{ESR}}}{\gamma_{NV}}. \tag{2.3}$$

Iso-field imaging is a useful technique to acquire magnetic contrast images in a short time. However, such images only depict magnetic structures qualitatively. For a quantitative measurement the magnetic stray fields are first mapped out with ODMR measurements and afterwards transformed into the corresponding magnetization using two different methods as described in the section below.

2.3 Determining the Surface Magnetization

It is possible to determine the magnetization $\sigma(x, y, z = 0)$ of a sample from the measured magnetic field $B_{\text{NV}}(x, y, h_{\text{NV}})$ along the NV-axis, if the magnetization of the sample is uniaxial [28]. This calculation is performed in Fourier space, where the measured field is directly related to $\sigma(k_x, k_y, 0)$, the Fourier transform of the real space magnetization. Lucas Thiel has implemented this *reverse propagation method* based on [28, 29]. A brief description is given below and more details can be found in the supplementary information of [4].

It can be shown that the field above a perpendicularly magnetized thin film can be written in Fourier space as [4]:

$$\mathbf{H}(\mathbf{k}, z) = -\nabla \left(\frac{\sigma(\mathbf{k}, 0)}{2} e^{-kz} \right), \tag{2.4}$$

where $\nabla = (ik_x, ik_y, -k)$ and $\sigma(\mathbf{k}, 0) = \sigma(k_x, k_y, 0)$ is the magnetization is Fourier space. With the relation $B = \mu_0 \cdot H$, the in-plane ($B_{x,y}$) and perpendicular (B_z) components of the magnetic field in Fourier space are then:

$$B_{x,y}(\mathbf{k}, z) = -\mu_0 \cdot ik_{x,y} \cdot \frac{e^{-kz}}{2} \cdot \sigma(\mathbf{k}, 0) =: T_{x,y} \cdot \sigma(\mathbf{k}, 0), \tag{2.5}$$

$$B_z(\mathbf{k}, z) = \mu_0 \cdot k \cdot \frac{e^{-kz}}{2} \cdot \sigma(\mathbf{k}, 0) =: T_z \cdot \sigma(\mathbf{k}, 0). \tag{2.6}$$

Rewriting the magnetic field along the NV-axis in Fourier space with B_x, B_y and B_z yields:

$$\begin{aligned} B_{NV}(\mathbf{k}, h_{NV}) &= \sin(\theta_{NV})\cos(\phi_{NV}) \cdot B_x + \sin(\theta_{NV})\sin(\phi_{NV}) \cdot B_y + \cos(\theta_{NV}) \cdot B_z \\ &=: T_{NV}(h_{NV}, \phi_{NV}, \theta_{NV}) \cdot \sigma(\mathbf{k}, 0), \end{aligned} \tag{2.7}$$

where h_{NV} is the NV to sample distance and ϕ_{NV} and θ_{NV} describe the NV orientation: ϕ_{NV} is the azimuthal angle in the x-y-plane and θ_{NV} is the angle with respect to the z-axis, which for NV centers in [001] oriented diamond tips is $\theta_{NV} = 54.7°$. Equation 2.7 shows that in Fourier space B_{NV} is linearly related to the magnetization $\sigma(k_x, k_y, 0)$. However, solving for $\sigma(k_x, k_y, 0)$ using Eq. 2.7 exponentially enhances high-frequency components and hence noise since the field $B_{NV}(\mathbf{k}, h_{NV})$ will be divided by the term e^{-kz} from Eqs.2.5, 2.6, i.e. it will be multiplied by e^{+kz}. The use of a low-pass filter function $W(k)$, as described in [4], solves

this problem. Rewriting Eq. 2.7 including the filter function $W(k)$ yields an expression for $\sigma(\mathbf{k}, 0)$:

$$\sigma(\mathbf{k}, 0) = \frac{W(k) \cdot B_{NV}(\mathbf{k}, h_{NV})}{T_{NV}(h_{NV}, \phi_{NV}, \theta_{NV})}. \tag{2.8}$$

In the following part we list the individual steps of the reverse propagation method implemented in this work:

- First, at each point of the scan the measured ODMR curves are fitted and the electron spin resonance frequency ν_{ESR} is determined. The field along the NV-axis is calculated via the relation:

$$B_{NV}(x, y, h_{NV}) = \frac{|\nu_{ESR} - D_0|}{\gamma_{NV}} - B_{\text{Bias-NV}}, \tag{2.9}$$

  where $\mathrm{D_0} = 2870\,\mathrm{MHz}$ is the zero field splitting, γ_{NV}=27.9 MHz mT^{-1} is the gyromagnetic ratio and $B_{\text{Bias-NV}}$ is the externally applied magnetic field along the NV-axis.

- Second, the magnetic field $B_{NV}(x, y, h_{NV})$[1] is two-dimensionally transformed into Fourier space: $B_{NV}(k_x, k_y, h_{NV})$.

- In Fourier space $B_{NV}(k_x, k_y, h_{NV})$ is related to the magnetization $\sigma(k_x, k_y, 0)$ via Eq. 2.8. Inserting guess parameters for the NV to sample distance $\mathrm{h_{NV}}$ and the angles ϕ_{NV} and θ_{NV} (which can both be measured with the field coils in our cryostat) in the tensor T_{NV} allows for the calculation of $\sigma(k_x, k_y, 0)$.

- Afterwards, $\sigma(k_x, k_y, 0)$ is transformed back to real space $\sigma(x, y, 0)$ and the domain boundaries are found. All areas of the sample are then assigned to a homogeneous magnetization value $\sigma_{\text{approx}} = \sigma_0 \cdot \text{sign}(\sigma(x, y, 0))$, where σ_0 is the monolayer magnetization.

- The magnetization σ_{approx} is then Fourier transformed into k-space. By comparing $\sigma_{\text{approx}}(k_x, k_y, 0)$ to the original data set, fit values for h_{NV}, ϕ_{NV} and θ_{NV} can be extracted with a least square fitting routine. These fitting parameters are then used to calculate $\sigma_{\text{final}}(k_x, k_y, 0)$ via Eq. 2.8.

- Finally, $\sigma_{\text{final}}(k_x, k_y, 0)$ is back transformed into real space to obtain $\sigma(x, y, 0)$.

The reverse propagation method allows to transform the measured field along the NV-axis B_{NV} into a homogeneous magnetization map. In order to independently determine the magnetization σ along the z-axis with an alternative method, we employ analytical fits to line cuts of the magnetic field over a flake edge [30, 31]. The outcome of the latter protocol are fitted values for the angles ϕ_{NV}, θ_{NV}, the NV-to-sample distance $\mathrm{h_{NV}}$ and the magnetization σ.

After having discussed the underlying principles of NV magnetometry, we will focus on the implementation of the measurement technique and the studied devices in the next chapter.

[1] For all data sets, which did not contain the entire flake within the scan range, the magnetic field data $B_{NV}(x, y, h_{NV})$ was extended outwards with a Gaussian drop-off to zero. This is necessary because our reverse propagation method assumes that no magnetic sources are present outside the scan range. If this condition is violated, additional (undesired) frequencies appear in the Fourier transformation. Therefore, the reverse propagation yields more reliable values for σ if the magnetic structure is entirely depicted in the scan range.

3 Setup and Devices

In this chapter we focus on the experimental setup and the geometry of our devices. In the first section of this chapter, Sect. 3.1, the measurement apparatus is described. Afterwards in Sect. 3.2, we present the studied CrI_3 devices.

3.1 Measurement Apparatus

Magnetic imaging of the devices was carried out in a low temperature AFM with a diamond scanning probe: A single NV quantum sensor is embedded in a diamond pillar, which scans the sample surface, as illustrated in Fig. 3.1. While the diamond tip records the topography of the device during a scan, the NV center is continuously probed with laser light and measures magnetic fields. The magnetometry measurements were performed in a liquid helium (He) bath cryostat (attoLIQUID 1000), as depicted in Fig. 3.1a, with a measurement temperature of $\sim 7\,\mathrm{K}$ due to microwave heating. A built-in three-dimensional vector magnet allows us to apply magnetic fields up to 0.5 T in all directions. We assured that neither the microwave power nor the green laser light induced any significant back-action onto the sample, c.f. Appendix B. Optical access to the NV center is provided by a home-built confocal microscope, which is placed on top of the cryostat.

Diamond Scanning Probe

The diamond scanning probe we employed in our experiments was fabricated by Lucas Thiel and Dominik Rohner. Since the nano fabrication was not part of this Thesis only a short description is given here and more details are provided in [33].

As a first fabrication step, nitrogen atoms were implanted into a chemical vapor deposition (CVD) grown diamond plate. Upon annealing, NV centers start to form and stabilize in the diamond lattice. Afterwards, electron beam and optical lithography together with multiple etching steps were used to fabricate the cantilever structures including the diamond pillars. As a part of this Thesis, individual devices were characterized and a suitable tip containing only one single NV center was chosen. The coherence function $g^{(2)}(\tau)$ was measured to identify single NVs, c.f. Appendix A. In a next step the cantilever (c.f. Fig. 3.1c) was glued to a quartz tip. The quartz tip was then attached to the tuning fork of the AFM head, see Fig. 3.1b. This configuration allows for topography measurements of the sample surface while the NV center can constantly be addressed and read out optically.

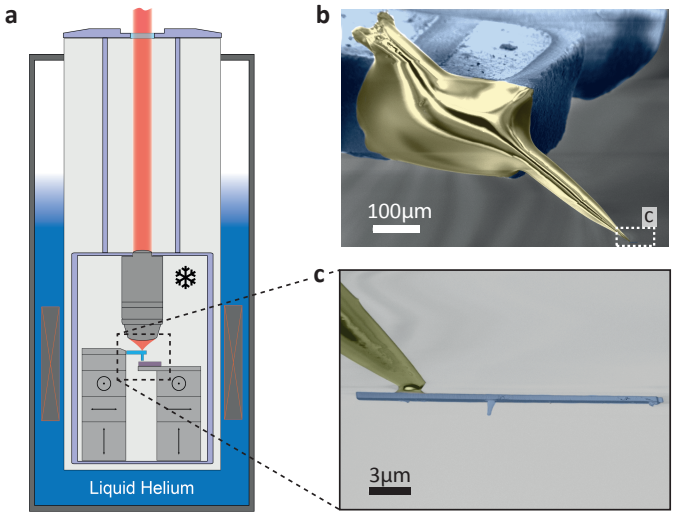

Figure 3.1: **Atomic force microscope (AFM) with a diamond scanning probe.** **a** Measurements were performed at ∼7 K in a low-temperature liquid helium (He) cryostat. The diamond scanning probe and the device are placed on two separate three-axis stages and optical access to the NV is provided by a confocal microscope on top of the cryostat (not depicted here). Schematic taken from [32]. **b** Representative false-color electron beam image of a quartz tip (golden), which is attached to a tuning fork at one end and to the diamond cantilever (white dashed box) at the other end. **c** Diamond cantilever (blue), which is glued to a quartz tip. The NV center is embedded in the bottom of the diamond pillar. Images **b** and **c** are taken from [33].

Optics and Microwave Circuit

As discussed in the previous chapter (Sect. 2.2), above-resonance light (532 nm) and microwave signals are required to initialize, manipulate and readout the NV spin. In this section the main parts of the optical setup and the microwave circuit are reviewed. A schematic of the experimental setup is shown in Fig. 3.2. The optical setup is assembled out of three main components:

1. The acousto-optic modulator (AOM) setup together with an arbitrary waveform generator (AWG), which enables control of the laser light intensity and pulsing.

2. The confocal microscope, which guides green laser light to the NV center and sends back the red fluorescence through a dichroic mirror.

3. The avalanche photodiode (APD) for measuring single photons emitted from the NV center.

First, green laser light (532 nm, LaserQuantum, GEM532) is sent through fiber polarization controllers (Thorlabs FPC560), which are used to optimize the polarization of the beam. A subsequent polarizing beamsplitter (PBS) transmits p-polarized (parallel) light into a double-pass AOM system, which controls the intensity and pulsing of the laser light. Inducing strain in an AOM crystal modulates its refractive index, which leads to diffraction of the incoming light. This mechanism is used to control the laser beam: A pinhole after the AOM filters out the diffracted light from the first order such that the beam is only passed through the system if

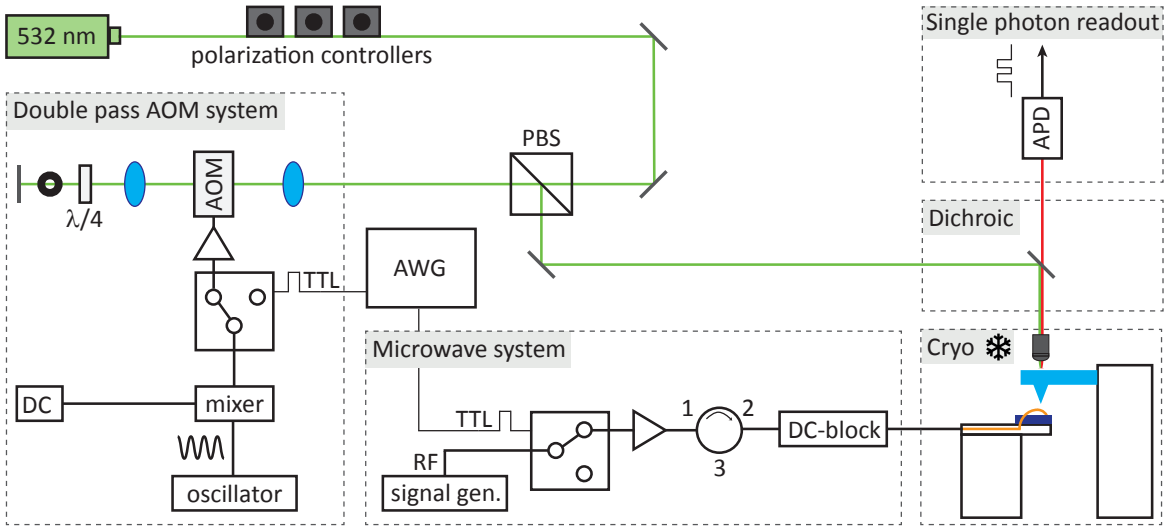

Figure 3.2: **Schematic of the setup.** Laser light (532 nm, green lines) is sent via a polarizing beam splitter (PSB) into a double pass acousto-optic modulator (AOM) system, which enables control of the laser intensity and pulsing. A dichroic mirror reflects off the green excitation light into the cryostat where it is focused on the NV center by an objective. The emitted photons (red line) are transmitted through the dichroic and captured by an single photon counting avalanche photo diode (APD). Spin manipulation of the NV center is achieved with microwave signals from a signal generator. The radio frequency (RF) signal is sent to a gold wire (orange), which is bonded over the sample and acts as an antenna.

the AOM is nominally "on". An AWG (Spectrum DN2.663-04) turns the AOM "on" and "off" via a switch, which transmits or blocks the input signal sent to the AOM. The input signal consist of the mixture of an oscillating signal from an oscillator (Mini-Circuits, ZX95-209-S+) and a programmable analog direct current (DC) voltage. The latter sets the laser intensity since the maximal DC signal yields largest possible diffraction of the light into the first order. Furthermore, two lenses are used to minimize the beam waist in the AOM, which allows for a minimal rise time ($\sim$ 13 - 23 ns, AOM Crystal Technology, Inc. Model 3200-146). A $\lambda/4$-plate behind the AOM changes the polarization of the light from p- to s-polarized (perpendicular) since the beam passes the plate twice upon reflection on a mirror. The s-polarized light is then reflected off the PBS and guided via a fiber to a confocal microscope and to the NV center. A built-in dichroic mirror reflects the green light and transmits the red NV fluorescence. Finally, the emitted photons are sent to an APD (Excelitas, SPCM-AQRH-13), which converts single photons to electric pulses. Digital acquisition cards (National Instruments) together with MATLAB software are used for data acquisition and scan control.

In order to drive the NV transitions with microwaves, a gold wire ($\varnothing$= 25 µm) is bonded over the sample and serves as an antenna. Microwaves are generated from a signal generator (Stanford Research Systems, SG386), amplified (Mini-Circuits ZVA-183W-S+) and sent through a circulator and DC block to the antenna. The circulator prevents reflected signals coming from the antenna from re-entering into the amplifier and the DC block filters out any remaining DC components in the radio frequency (RF) signal. A switch and the AWG enable control over the microwave pulse length.

3.2 Devices

The devices we study in this work were fabricated in Geneva in the group of Prof. Alberto Morpurgo. Single CrI_3 crystals were grown by the Chemical Vapor Transport method or purchased from the company HQ graphene. The material was handled in the inert atmosphere of a glovebox. CrI_3 flakes were first exfoliated from the bulk crystals and subsequently encapsulated in either graphene (3 - 10 nm) or hexagonal boron nitride (hBN) (5 - 20 nm) to avoid degradation of CrI_3 in air. The number of layers of a flake was determined via the relative optical contrast between the CrI_3 crystals and the 90 nm silicon dioxide (SiO_2) substrate. Additionally, AFM measurements were performed on the encapsulated flakes. In this work we investigated magnetism in three different CrI_3 samples: A monolayer sample (CrI_3 from HQ graphene), a bi- and tri-layer sample (self-grown CrI_3) and a few-layer sample (self-grown CrI_3). In the sections below we present optical images of the devices, qualitative iso-field scans and AFM measurements. Thereafter, the quantitative magnetic imaging data will be discussed in Chap. 4.

Monolayer Device

Fig. 3.3a shows an optical image of the exfoliated monolayer device D_1. The single layer is attached to a bi-layer flake next to two thicker pieces of CrI_3 (greenish color). The material was encapsulated with graphene. During the encapsulation process bubbles between the different

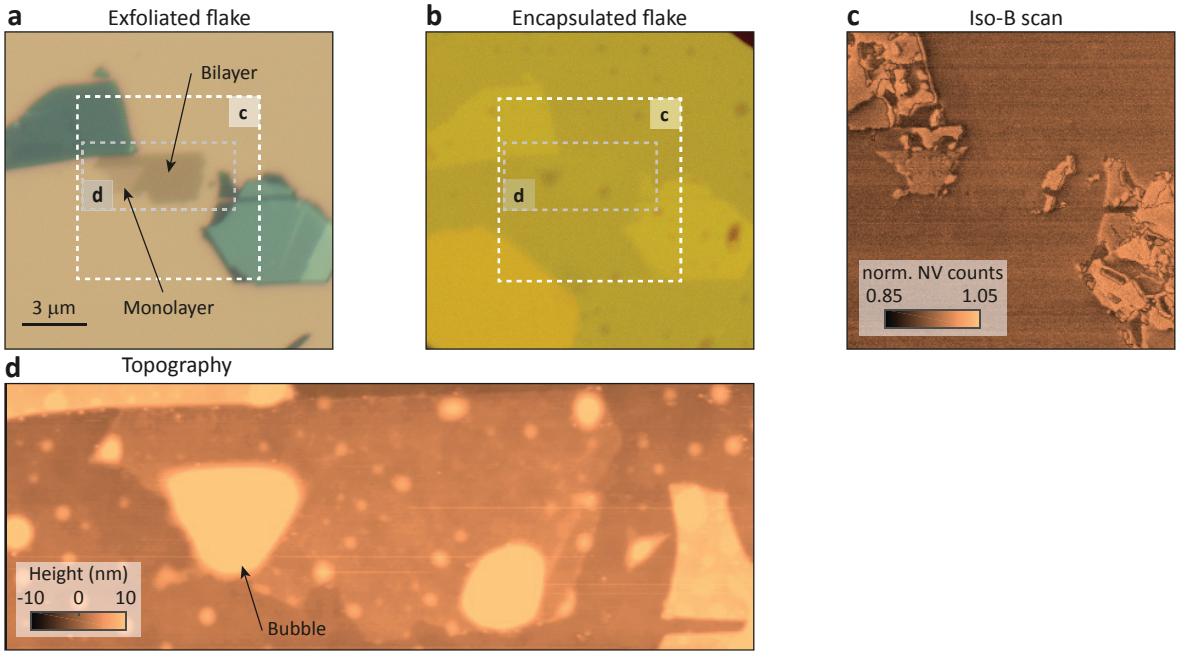

Figure 3.3: **Monolayer device D_1. a** Optical image of the exfoliated monolayer flake. The single layer is attached to a bilayer flake and encapsulated with graphene as shown in **b**. **c** Iso-field scan ($B_{iso} = 0.27$ mT, integration time = 0.8 s) of the area illustrated with a white dashed box in **a** and **b**. **d** AFM measurement of the encapsulated device. The figures were created by Lucas Thiel and taken from the supplementary information of [4] and are slightly modified here.

materials can emerge, as visible as dark spots in Fig. 3.3b. The iso-field scan of sample D_1 shows magnetic contrast from the monolayer region and the thicker CrI_3 parts but no magnetic field from the bi-layer part, c.f. Fig. 3.3c. The scanned area of Fig. 3.3c is illustrated with a white dashed box in Fig. 3.3a. Interestingly, the AFM image in Fig. 3.3d reveals that the monolayer part was covered by a bubble, which is further discussed in Sect. 4.1.1.

Bi- and Tri-layer Device

The bi- and tri-layer device $D_{2,3}$ is shown in Fig. 3.4. In the optical microscope picture in Fig. 3.4a the two- and three-layer regions are visible. The device was encapsulated with graphene, as shown in Fig. 3.4b. The iso-field scan in Fig. 3.4c was taken while a magnetic domain was induced in the sample after first applying a negative field of $B_z = -495\,\mathrm{mT}$ and then changing the field to $B_z = +91\,\mathrm{mT}$. The region of the iso-field scan is indicated in Fig. 3.4a with a white dashed box. Figure 3.4d shows an AFM measurement of $D_{2,3}$ and the line cut plotted in Fig. 3.4e confirms the thickness of the flake to be around 2.1 nm, as

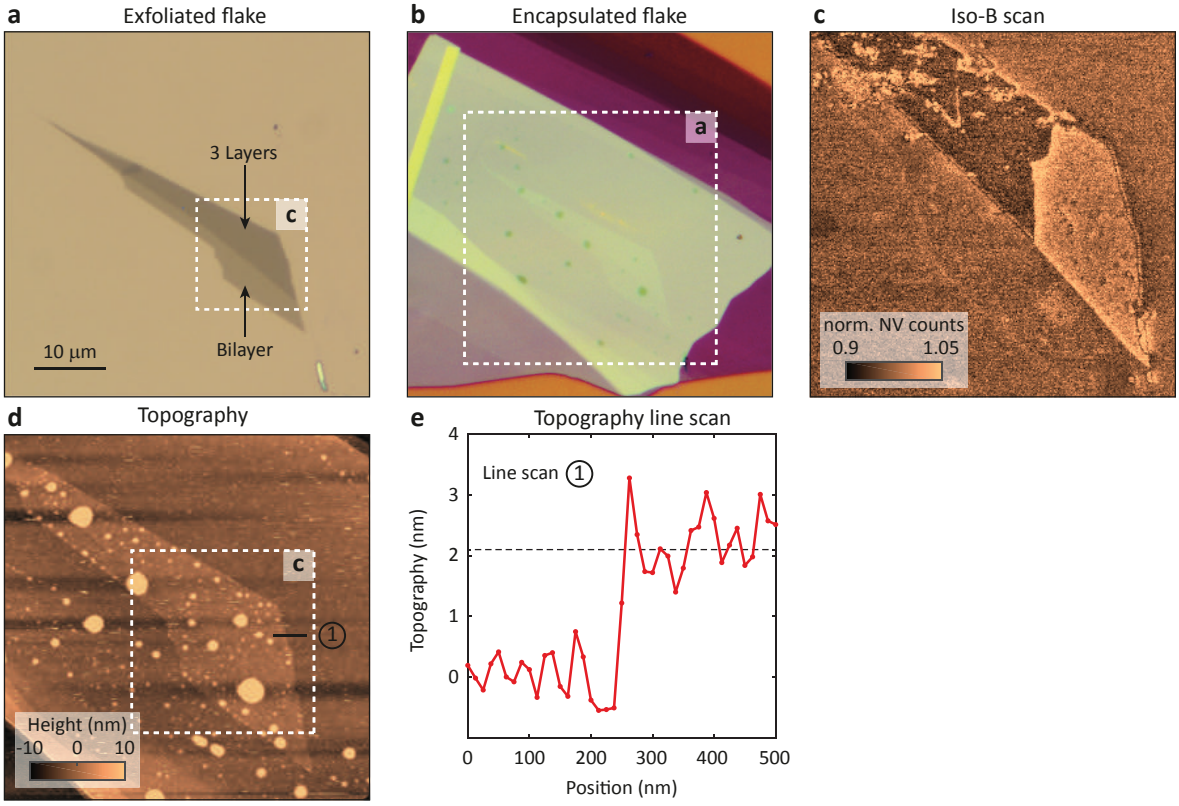

Figure 3.4: **Bi- and tri-layer device $D_{2,3}$. a** Optical image shows the two layer part adjacent to the three layer region. **b** Optical image of the encapsulated device. Encapsulation: graphene. The white dashed box indicates the image section of **a**. **c** Iso-field scan ($B_{\mathrm{iso}} = 0.12\,\mathrm{mT}$, integration time $= 0.2\,\mathrm{s}$) of sample $D_{2,3}$ after a domain was induced. The scanned area is highlighted in **a** with a white dashed box. **d** The sample's topography was measured with AFM. The line cut denoted with ① is plotted in **e** together with the expected thickness of for a three-layer flake of 2.1 nm (black dashed line). Figures created by Lucas Thiel, taken from [4] and slightly modified.

expected for three 0.7 nm thick CrI_3 layers.

Few-layer device

The third sample we study in this Thesis is a few-layer device $D_{5,9}$ with a five- and a nine-layer part as shown in the optical image of Fig. 3.5a. For this sample hBN was used for the encapsulation, c.f. the optical microscope image in Fig. 3.5b. The iso-field image of $D_{5,9}$ is plotted in Fig. 3.5c. During one of the scans a hole was punctured into the device, as discussed in Sect. 4.2.1. The data in Fig. 3.5c was taken before the puncture. The topography of the few-layer sample after the puncture is shown in Fig. 3.5d. The puncture occurred in the upper right corner of the nine-layer region. Two line cuts confirm the thickness of five layers to be ~ 3.5 nm (line scan 1) and the difference of four layers between the five and nine-layer part to be ~ 2.8 nm (line scan 2).

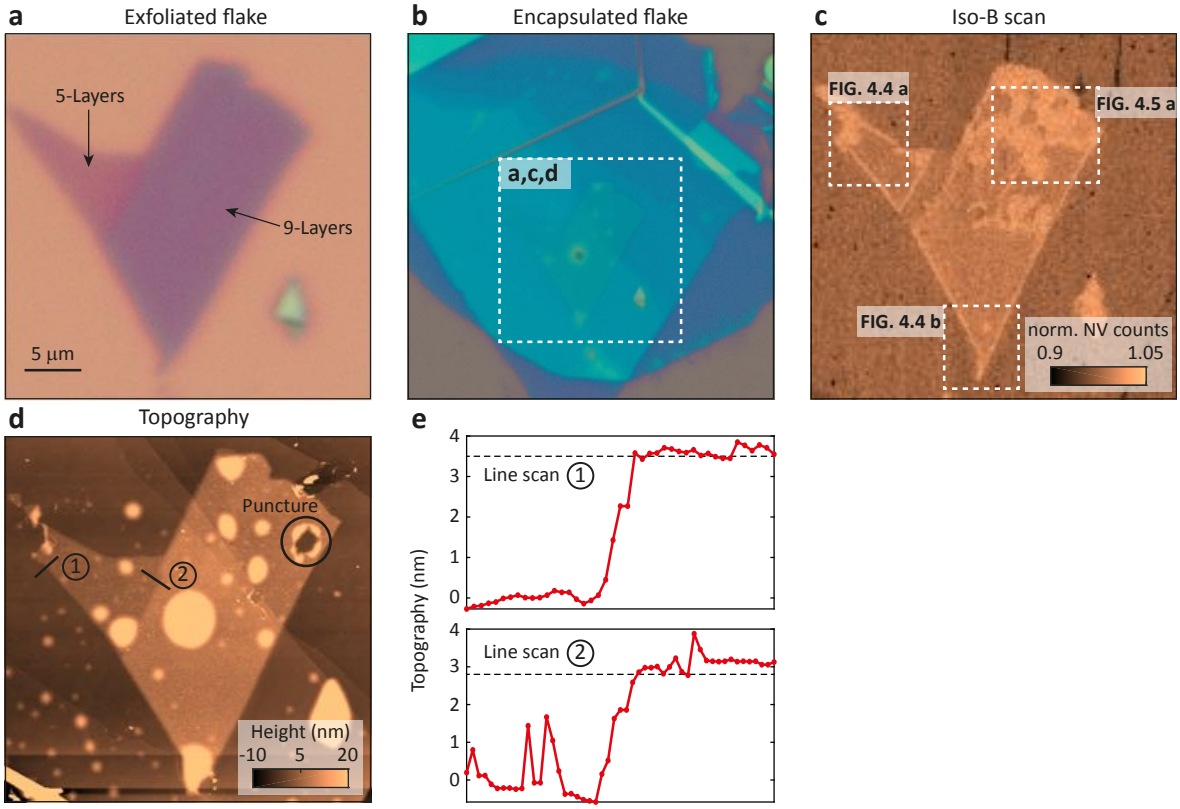

Figure 3.5: **Few-Layer device $D_{5,9}$.** **a** The five and nine layer regions of sample $D_{5,9}$ are visible in the optical microscope picture. **b** Sample $D_{5,9}$ was encapsulated in hBN. The white dashed box denotes the image and scan sections of **a**, **c** and **d**. **c** Iso-field scan ($B_{\mathrm{iso}} = 0$ mT, integration time $= 0.18$ s) of sample $D_{5,9}$ before the puncture of a hole. **d** AFM topography after the hole was punctured into the device. Line scans in **e** show the thickness of five (line scan 1) and 9-5 = 4 (line scan 2) layers together with the expected thicknesses (black dotted lines) of 3.5 nm and 2.8 nm respectively. Figures created by Lucas Thiel, taken from [4] and slightly modified.

4 Results

In this chapter we discuss our findings on magnetism in the vdW magnet CrI_3. An NV scanning probe technique for quantitative magnetic imaging is employed to study the even-odd effect (antiferromagnetic interlayer exchange coupling) in Sect. 4.1. Subsequently, in Sect. 4.2 we present evidence for a correlation between the stacking order and magnetic phase in CrI_3. In the last part of this chapter, Sect. 4.3, magnetization reversal and domain nucleation in thin CrI_3 are described.

4.1 Antiferromagnetic Interlayer Coupling in CrI_3

Experiments on encapsulated CrI_3 flakes at low temperatures suggest that the interlayer coupling in this vdW magnet is of antiferromagnetic nature – instead of ferromagnetic as expected from DFT calculations [3, 17] (c.f. Chap. 2). Antiferromagnetic interlayer coupling would imply zero stray field emerging from even numbers of CrI_3 layers and a net magnetization of one fully polarized layer for odd numbers of layers. This peculiar *even-odd effect* in few layer CrI_3 has yet to be studied and verified using a quantitative measurement technique. Here, we investigate the interlayer exchange coupling in CrI_3 with an NV scanning probe for quantitative magnetic imaging at the nanoscale. We report on the results of measurements on three different devices D_1, $D_{2,3}$ and $D_{5,9}$: First, in Sect. 4.1.1 a monolayer sample (D_1) is studied. Next, we discuss the magnetic field measured above a flake with bi- and tri-layer areas (sample $D_{2,3}$) in Sect. 4.1.2. Finally, a few-layer flake with five and nine layer sections (sample $D_{5,9}$) is examined in Sect. 4.1.3.

The standard procedure we apply for magnetic imaging is to acquire ODMR spectra at different points in a plane above the sample. From this dataset the magnetic stray field along the NV-axis can be calculated, c.f. Sect.2.2. Using the reverse propagation technique described in Sect.2.3, the surface magnetization of the sample is determined. Typical measurement parameters employed in the datasets and frequently used abbreviations are summarized in the table 4.1.

$\sigma_{\text{mono,theor}} = 14.7\ \mu_B/\text{nm}^2$	Expected magnetization of one fully polarized CrI_3 layer [7]
$B_{\text{Bias-NV}} \sim \pm\ 172.5\,\text{mT}$	External field along NV-axis (optimizes ODMR contrast)
$P_{\text{laser}} \sim\ 40\,\mu\text{W}$	Power of the green excitation laser
$h_{\text{NV}}\ \sim 60\,\text{nm}$	Typical NV-to-sample distance

Table 4.1: Commonly used parameters in our experiments.

4.1.1 Monolayer CrI_3

To study the magnetization of a monolayer CrI_3 flake (monolayer sample D_1: see Sect. 3.2), we first cooled the sample down to ~ 7 K in zero magnetic field. Afterwards, the external field was set to $B_{\text{Bias-NV}}$=172.5 mT for an iso-field image and thereupon the field was decreased back to zero, where a two-dimensional ODMR map of sample D_1 was acquired. At zero external magnetic field a small residual magnetization of $B_{\text{Bias-NV}}$=0.15 mT was observed, possibly arising from, for example, a small current still present in the coils of the superconducting magnets or a slight magnetization of components of the setup (such as the objective).

In Fig. 4.1a the measured magnetic stray field along the NV symmetry axis is plotted ($B_{\text{Bias-NV}}$=0.15 mT). The prominent red (blue) edges results from positive (negative) projections of the stray field along the NV-axis as the tip is scanned across the flake. We deduce the magnetization of the flake from the stray field map using the reverse propagation method described in Sect. 2.3. The magnetization map of the monolayer flake is shown in Fig. 4.1b. The nearly homogeneous magnetization is comparable to the theoretically expected value of 14.7 μ_B/nm^2 for a monolayer [7]. On the right side of the monolayer flake a negatively polarized CrI_3 region is visible. However, this negative magnetization could possibly be a measurement artifact, as we may have tracked the wrong NV spin transition after the m_s=0 to m_s= ±1 transition frequencies have crossed at zero field. If that was the case indeed, any positive field would have wrongly been interpreted as a negative field in this region. To resolve such an uncertainty an ODMR map has to be acquired at a higher external magnetic field where the two NV transition frequencies (m_s=0 to m_s= +1 and m_s=0 to m_s= -1) cannot cross.

Furthermore, the dataset from Fig. 4.1a is noisy due to small ODMR contrast (about 3%) at almost zero external field. Therefore, the fits of the electron resonance frequency ν_{ESR} in the ODMR spectra were rather poor, which made it difficult to transform the frequency map into a reliable magnetic field map. Measuring the NV contrast as a function of external magnetic field showed that working at $B_{\text{Bias-NV}} \sim \pm 172.5$ mT (in z-direction B_z=91.5 mT) yields the best ODMR contrast (∼18%, see Appendix C). To date we do not understand why the ODMR contrast changes significantly as a function of applied magnetic field in our cryostat. One hypothesis is that the superconducting magnet generates more magnetic noise

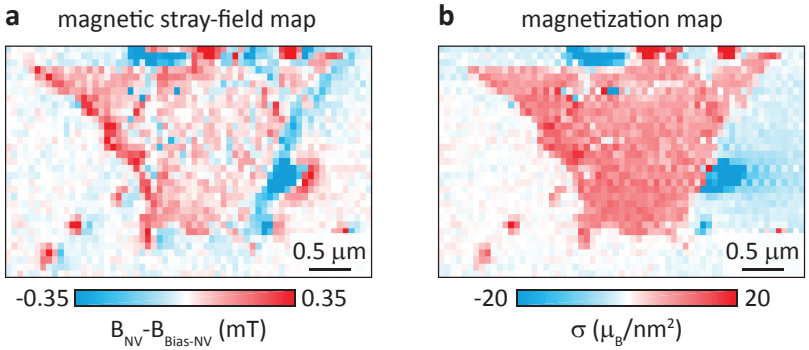

Figure 4.1: **Monolayer CrI_3 flake imaged in a small external field $B_{\text{Bias-NV}}$= 0.15 mT.** **a** Magnetic field along the NV-axis calculated from the ODMR resonances. **b** Monolayer magnetization map obtained from the reverse propagation method.

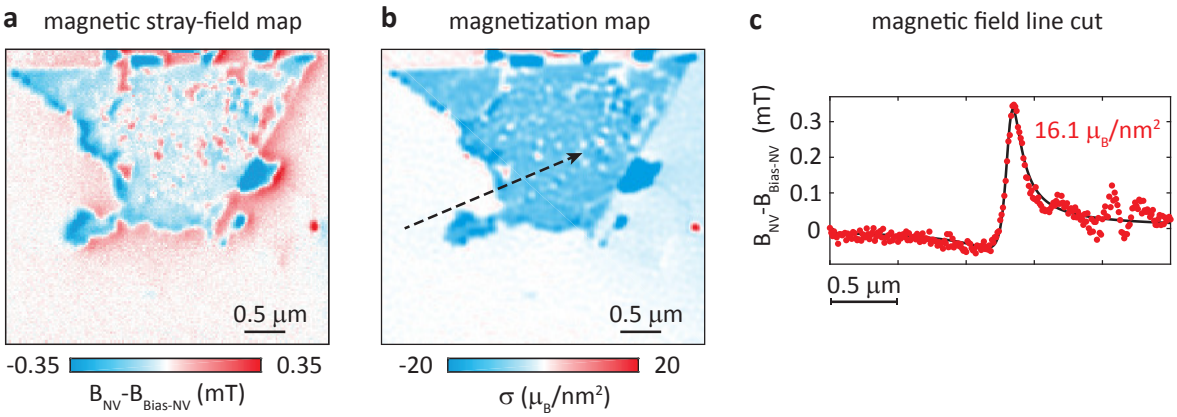

Figure 4.2: **Monolayer CrI_3 flake imaged in $B_{Bias\text{-}NV}$=−171 mT. a** Magnetic field along the NV-axis, relative to the external field $B_{Bias\text{-}NV}$. **b** Magnetization map of the monolayer flake. Black arrow denotes the position of the line cut plotted in **c**. Fitting the the line cut determined the monolayer magnetization σ=16.1 μ_B/nm^2. Stray field data from the line cut was inverted to obtain a positive value for σ. Images created by Lucas Thiel and taken from [4].

at small fields. This would lead to a reduction in the NV spin relaxation time T_1, the time-scale on which a polarized NV spin state decays into thermal equilibrium [22], and would hence make ODMR measurements inefficient. In the future it would be important to study the reason for the dependency of the ODMR contrast on the applied magnetic field. In our experiments, the ODMR spectra were usually acquired in an external magnetic field applied along the NV-axis, which was later subtracted from the dataset for analysis. Working in external fields did not disturb our measurements of the even-odd effect since the critical field required to magnetize bi-layer CrI_3 is around 600 mT [3], which is above the maximal field of 500 mT we can apply with our magnet.

Figure 4.2a shows a high resolution two-dimensional scan of the monolayer CrI_3 flake measured in a field $B_{Bias\text{-}NV} = -171$ mT. The spatial resolution of the scans is limited by the NV-to-sample distance h_{NV} [27], which was typically $\sim$ 60 nm in our experiments (determined from fits to line cuts, c.f. Fig. 4.2c). From the reverse propagation method we obtain the magnetization map shown in Fig. 4.2b. Again we observe a magnetization comparable to $\sigma_{mono,\,theor}$. To independently determine the magnetization with a different method, we took a line cut across the sample edge (black arrow in Fig. 4.2b) and fitted the corresponding stray field data to an analytical fit [30, 31]. As a result we obtain a magnetization of 16.1 μ_B/nm^2.

The monolayer magnetization resulting from our data sets in Fig. 4.1b and Fig. 4.2b are comparable to the theoretically expected value of $\sigma_{mono,theor}$=14.7 μ_B/nm^2. To verify if antiferromagnetic interlayer coupling is present in multi-layer (n_{layers} >1) CrI_3 we determined the magnetization of a bi- and tri-layer CrI_3 flake, as described in the next section.

4.1.2 Bi- and Tri-layer CrI_3

We imaged the magnetic stray field resulting from a bi-layer region of CrI_3 adjacent to a tri-layer region (sample $D_{2,3}$: see Sect. 3.2). If antiferromagnetic interlayer exchange coupling

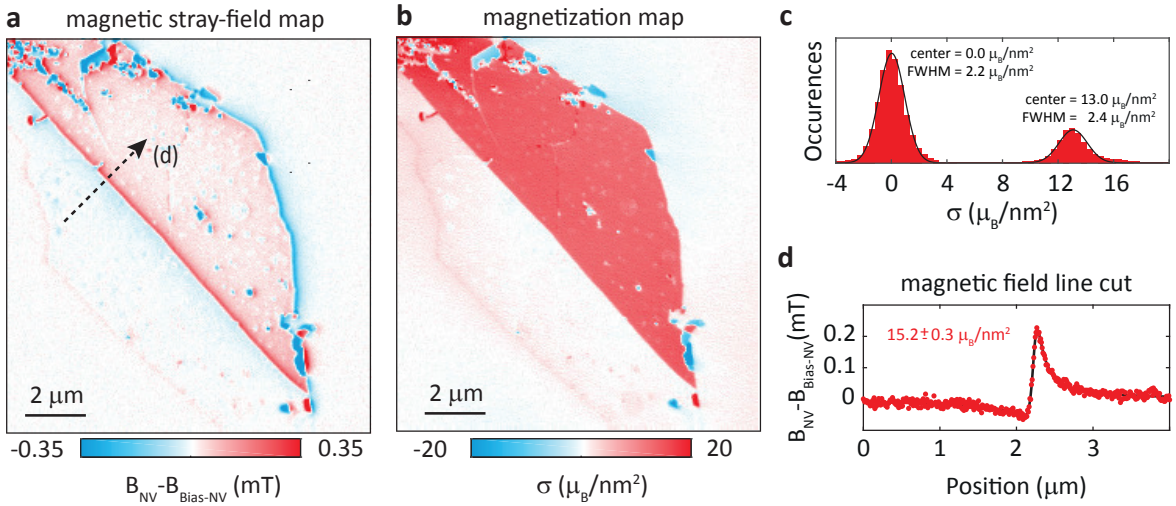

Figure 4.3: **Magnetism in bi- and tri-layer CrI_3.** **a** Magnetic stray field of sample $D_{2,3}$. Data recorded at $B_{Bias\text{-}NV}$=172.5 mT. The black dotted arrow indicates the location of the line cut plotted in **d**. **b** Magnetization map obtained via the reverse propagation method. **c** Histogram of the magnetization values on the tri-layer part shows an average magnetization of σ=13.0 μ_B/nm^2. **d** A fit to the line cut of the magnetic field along the NV-axis (black dotted arrow in **a**) independently determines σ=15.2 μ_B/nm^2. Figures originally created by Lucas Thiel. Taken from [4], rearranged and slightly modified.

is present in CrI_3 we would expect the tri-layer part to show a magnetization of one fully polarized CrI_3 layer and zero stray field from the bi-layer part.

In Fig. 4.3a the magnetic stray field along the NV-axis is plotted. The data was taken in an external magnetic field of $B_{Bias\text{-}NV}$=172.5 mT, which was subtracted from the dataset in Fig. 4.3a. A strong signal arises predominantly at the edges of the flake, as expected for a uniformly magnetized layer [30]. This indicates that the tri-layer part exhibits a stray field, which is in good agreement with antiferromagnetic interlayer coupling. Moreover, no comparable stray field emerges from the bi-layer area. A very faint signal along the bi-layer flake edge is visible. The origin of this small field is not understood so far. It may be caused by a narrow monolayer part protruding at the flake edge or by magneto-electric effects [34], where local electric fields can influence magnetism in bi-layer CrI_3.

Using the reverse propagation method we deduce the magnetization map shown in Fig.4.3b. On the tri-layer part an average magnetization of 13.0 ± 2.4 μ_B/nm^2 is found and the bi-layer region shows no net magnetization, c.f. the histogram in Fig. 4.3c. Additionally, the magnetization was independently determined via an analytical fit to a line cut across the tri-layer sample edge (c.f. black dotted arrow in Fig. 4.3a) plotted in Fig. 4.3d. The fit yields a value of σ=15.2 ±0.3 μ_B/nm^2.

We observe a magnetic signal from the tri-layer part with a field-strength comparable to $\sigma_{\mathrm{mono,theor}}$ and no net field from the bi-layer. These findings are in perfect agreement with antiferromagnetic interlayer coupling. To further validate the presence of the even-odd effect in CrI_3 we next study another multi-layer device (n_{layers} >3).

4.1.3 Few-layer CrI_3

To verify whether the even-odd effect persists beyond three CrI_3 layers, we studied a few-layer ($n_{layers} < 10$ layers) sample with a nine layer and a five layer part (few-layer sample $D_{5,9}$, see Sect. 3.2). Figure 4.4a shows the magnetization of the five layer CrI_3 region obtained from the reverse propagation protocol. A line cut of the corresponding stray field (indicated by a black dotted arrow) across the sample edge was used to determine the surface magnetization σ, as shown in Fig. 4.4c: From the fit we find σ=16.4 μ_B/nm^2. In Fig. 4.4b the magnetization on a nine-layer CrI_3 flake is shown. Again, a line cut (black dotted arrow) was used to obtain the surface magnetization σ=14.1 μ_B/nm^2, as plotted in Fig. 4.4d. From both the five and the nine layer part, a magnetization comparable to the single layer magnetization was measured, as expected for antiferromagnetic interlayer coupling.

Even though the magnetization maps from Fig.4.4 are very homogenous, we nevertheless observe some magnetic defects, such as the circular structure in Fig. 4.4b in the middle of the flake. Small defects and inhomogeneities in the sample could originate from curling or wrinkling up parts of the flake during the fabrication process. Further studies on CrI_3 could investigate the nature of such defects.

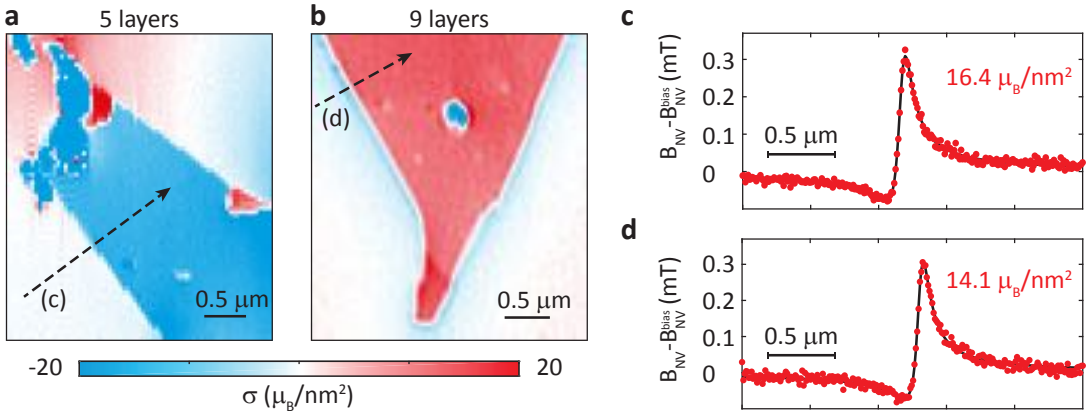

Figure 4.4: **Magnetism in five- and nine-layer CrI_3.** **a** Magnetization map of a five-layer part (**a**) and a nine-layer part (**b**). **c** and **d**: Line cuts across the sample edge (black dotted arrows) of the corresponding magnetic stray fields are plotted in red. The magnetization was determined by a fitting routine and the stray field from line cut (**c**) was inverted to obtain a positive value for σ.

Domain Regions

In another part of sample $D_{5,9}$ we observed a region with domains (c.f. iso-scan Fig. 3.5c in Sect. 3.2). Figure 4.5a shows the magnetization map of the corresponding area. We observe domains with a magnetization quantized to integer multiples of one monolayer magnetization σ_{mono}. A possible explanation for this observation is the occurrence of spatial variations of the exchange coupling in the flake in all three dimensions. Locally, the coupling between the layers could change from antiferromagnetic to ferromagnetic due to a change in crystal structure or stacking order.

Interestingly, in some areas of sample $D_{5,9}$ only even or odd multiples of σ_{mono} are observed, as illustrated with dotted lines in Fig. 4.5a and confirmed by the histograms in

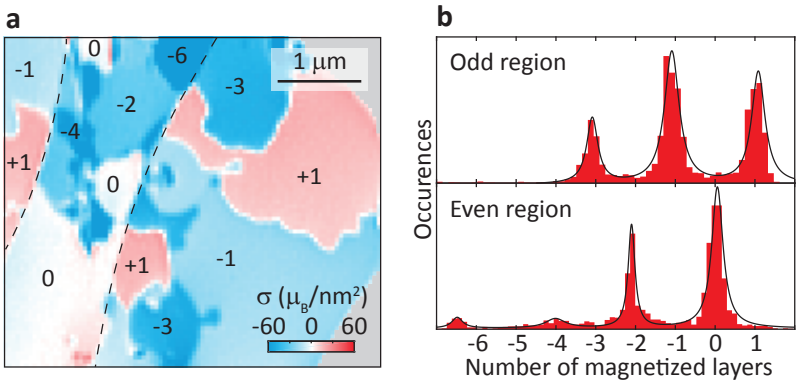

Figure 4.5: **Domain region in sample $D_{5,9}$. a** Domains with a magnetization quantized in even or odd integers of σ_{mono} are observed, which we attribute to local variations of exchange coupling in the material. **b** Histograms of the magnetization pattern in **a** confirm the occurrence of regions with only odd or only even multiples of σ_{mono}. Figure by Lucas Thiel and taken from [4].

Fig. 4.5b. We tentatively attribute the difference between even and odd σ_{mono} regions to the removal or addition of a piece of monolayer CrI_3, which may have occurred during the fabrication process.

The data in Fig. 4.5 suggest that the interlayer exchange coupling in CrI_3 can locally vary between antiferromagnetic and ferromagnetic. This could be explained by the correlation between crystal structure and magnetization, which we will further explore in the next section.

4.2 Controlling and Understanding Stacking Order in CrI_3

From literature it is known that CrI_3 arranges in two different structural phases: in the rhombohedral phase below 220 K and in the monoclinic phase for temperatures above [7]. DFT calculations have shown that in the low-temperature phase (rhombohedral) the interlayer exchange coupling is expected to be ferromagnetic, and antiferromagnetic interlayer coupling is expected for the high-temperature phase (monoclinic) (c.f. Sect.2.1). However, this prediction is in contradiction to measurements, which consistently found antiferromagnetic coupling in CrI_3 at low temperatures [3]. This raises the question of how the crystal structure of CrI_3 is related to the magnetization of the material and whether this can be controlled or not.

In this section we first discuss how we were able to induce a change from antiferromagnetic to ferromagnetic coupling in CrI_3 by a structural modification of the crystal (Sect. 4.2.1). Raman measurements were performed to distinguish between different crystal phases of CrI_3, which are also presented in Sect. 4.2.1. Subsequently, more detailed Raman studies on CrI_3 are discussed in Sect. 4.2.2. Finally, in Sect. 4.2.3 we present the idea of controlling the structural phase of CrI_3 by annealing of encapsulated flakes.

4.2.1 Switching from AFM to FM Stacking Order in CrI_3

The observed switch from antiferromagnetic to ferromagnetic coupling in CrI_3 was a fortunate accident: During one of the scanning probe imaging experiments, the diamond tip of our scanning probe unintentionally punctured a hole into the nine-layer CrI_3 flake as indicated

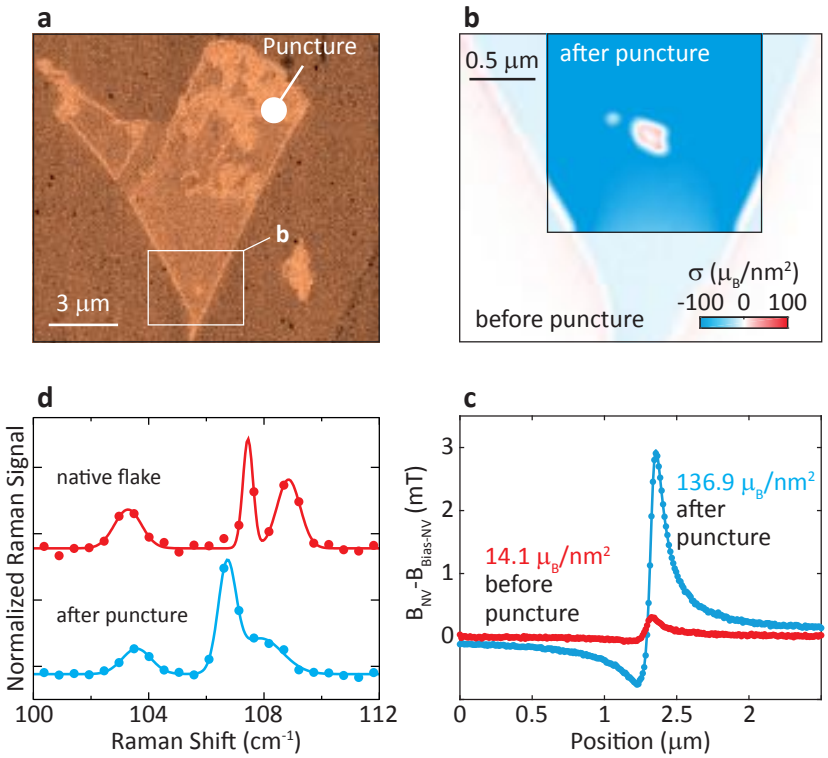

Figure 4.6: **Increase in magnetization upon structural modification of CrI_3. a** During a scan the diamond tip unintentionally punctured a hole into the nine-layer part (indicated with a white dot). **b** The magnetization of the nine-layer part (scan section of **b** is denoted with a white dashed box in **a**) increased after the puncture. **c** From fits to line cuts over the sample edge before (red line) and after (blue line) the puncture we deduce a factor of 9.7 increase in magnetization. **d** Unpolarized low-temperature Raman measurements confirm a structural difference between a native flake and the punctured flake. Figure created by Lucas Thiel and taken from [4].

by the white dot in Fig. 4.6a. An AFM measurement of the punctured device is shown in Fig. 3.5b. Upon the creation of this hole the sample magnetization increased by roughly a factor of nine.

Figure Fig. 4.6b shows the magnetization of the bottom part of the nine-layer CrI_3 flake (area indicated with white box in Fig. 4.6a). The faint colors represent the magnetization before the puncture and the inset of Fig. 4.6b illustrates the increase of magnetization in the same area after the puncture of the device. By fitting line cuts over the nine-layer sample edge (Fig. 4.6c) we conclude that the magnetization increased by a factor of ∼9.7.

Subsequent low-temperature Raman measurements show that the change in magnetization was related to a structural change of the CrI_3 flake. The Raman measurements on the flake after the puncture (Fig. 4.6d blue line) show a different spectrum compared to the Raman data taken on a native, unpunctured reference flake (Fig. 4.6d red line). The Raman peaks from the device after the puncture are closer to each other than the peaks from the native flake are. Also, the Raman peaks between 106 cm^{-1} and 109 cm^{-1} seem to merge into one peak after the change in magnetization. The changes in the Raman spectrum indicate a modification of the crystal structure of the material.

One possible explanation for the change in interlayer coupling from antiferromagnetic to ferromagnetic is that the structural modification released strain from the encapsulation, causing the sample to rearrange itself in the low-temperature phase with ferromagnetic interlayer coupling. However, it is important to note that we did not perform polarization-selective Raman measurements, and we can therefore not unambiguously verify that the flake is in the rhombohedral or monoclinic phase by comparing the Raman peaks to the literature (where polarization-selective Raman spectra are reported) [35].

Future studies should investigate the correlation between magnetic phase and structural order in CrI_3. To that end, low-temperature Raman spectroscopy performed in parallel to NV magnetometry could shed light onto the different structural phases of CrI_3. First attempts of obtaining more precise Raman spectra on few-layer CrI_3 are presented in the next section.

4.2.2 Raman Spectroscopy on few-layer CrI_3

As shown in the previous section, Raman spectroscopy is a useful tool to determine the crystal structure of encapsulated CrI_3 flakes. Whereas Raman studies on bulk and few-layer (> 10 layers) CrI_3 crystals have recently been reported [35, 36], this spectroscopy technique has not been established on very thin (< 10 layers) CrI_3 yet. Here, we present room-temperature Raman measurements on few-layer (~ 12 layers) and bi-layer CrI_3.

The Raman experiments on encapsulated CrI_3 were performed in the Nanophononics Group at the University of Basel, with the help of Dr. Marta De Luca. We excited the sample with the 514.5 nm line of an Ar^+- Kr^+ laser and the laser power was set to 0.5 mW to avoid heating or damaging effects. Using a high numerical aperture (NA = 0.8) 100x objective we achieved a spatial resolution of about 600 nm for the 514.5 nm laser (the laser spot size was measured to be ~ 600 nm). The polarization of both the incident laser light and of the backscattered beam were controlled and selected using polarization optics. In the parallel polarization (cross-polarization) mode, the incident laser beam is parallel (perpendicularly) polarized with respect to the backscattered beam. We collected the scattered light with a triple spectrometer with a 1800 g/mm grating and a liquid nitrogen-cooled CCD detector (spectral resolution between 0.5-1 cm^{-1}).

Raman spectra were measured on the bi-layer region and on a thicker flake of CrI_3 from sample D_1, as shown in Fig.4.7a. The device was encapsulated in graphene. We discuss the Raman spectra acquired on three different points across the sample:

- p1: Point on a thick $\sim$9 nm CrI_3 flake (~ 12 layers, height determined in an AFM).
- p2: Spot on the bi-layer region of sample D_1.
- p3: Reference point on the graphene encapsulation to distinguish between Raman peaks from CrI_3 and from the substrate.

The corresponding Raman spectra are shown in Fig.4.7b,c. An offset in intensity is observed due to background signal from light reflected directly off the sample surface. From the Raman spectra in Fig.4.7b we conclude that the signal at 107 cm^{-1} results from CrI_3. The corresponding Raman peak is strong on the thick flake and still visible on the bi-layer part, even though much weaker, as expected for thinner layers. The 107 cm^{-1} signal at p2 is

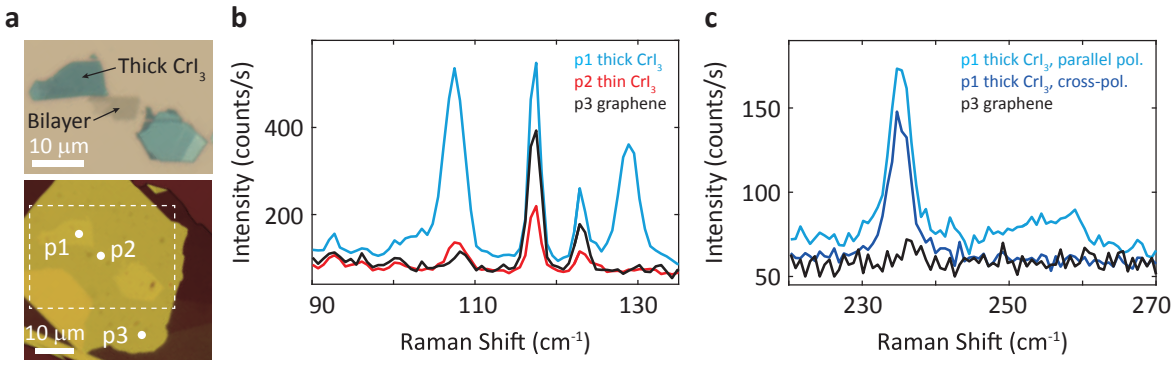

Figure 4.7: **Raman measurements on CrI_3 at room-temperature. a** Optical images of sample D_1 before (upper image) and after (lower image) encapsulation with graphene. White dashed box denotes the range of the upper image. Raman spectra were acquired at three different points: p1 was measured on a thick (∼9 nm, determined with AFM) CrI_3 flake, p2 was measured on the bilayer region of the sample and p3 is a reference point on the graphene encapsulation. **b** Raman spectra with parallel-polarization. **c** Raman spectra in a different spectral range with parallel and cross-polarization.

distinguishable from the reference point on graphene, since it has a slightly different center frequency and is stronger in intensity. Also, we attribute the Raman peak at 129 cm^{-1} to a signal from CrI_3 since no comparable peak is observed in the reference spectra and similar results were seen in [35]. The other two peaks in the spectra between 112 cm^{-1} and 125 cm^{-1} are probably related to yet not so extensively investigated low-frequency Raman modes in few-layer graphene [37]. Figure 4.7c shows the Raman spectrum in a different spectral range. A peak around 235 cm^{-1} was measured in both polarization detection modes (parallel- and cross-polarization), which is in good agreement to the results of Shcherbakov *et al.* in [36]. Additionally, a broad Raman peak at 250-260 cm^{-1} is measured in parallel polarization. The peak probably occurs from a 2-phonon-process and was also observed in [36].

Our Raman spectroscopy results on CrI_3 are promising: we observe similar Raman peaks for thick CrI_3 as reported in literature and we were furthermore able to acquire a signal from bi-layer CrI_3, which opens the way to the yet unexplored Raman studies on single layer CrI_3. In future experiments we hope to measure a stronger signal from bi-layer CrI_3 by increasing the laser power without damaging the flake. However, it remains a challenge to avoid the Raman peaks between 112 - 125 cm^{-1}, which we attribute to the graphene encapsulation. Possibly, these signals could vanish if very thin ($<$ 3 layer) graphene or hBN is used for encapsulation of future devices [37].

4.2.3 Annealing

As discussed in Sect.4.2.1, we would like to further investigate the correlation between structural modification and magnetic order in CrI_3. Especially, we are interested in examining why encapsulated CrI_3 flakes couple antiferromagnetically at low temperatures instead of ferromagnetically, as expected from DFT calculations, c.f. Sect. 2.1. One hypothesis is that strain of the encapsulation is responsible for keeping few layer CrI_3 in the monoclinic phase at low temperatures. This could possibly be tested with thermal annealing: We would like to verify

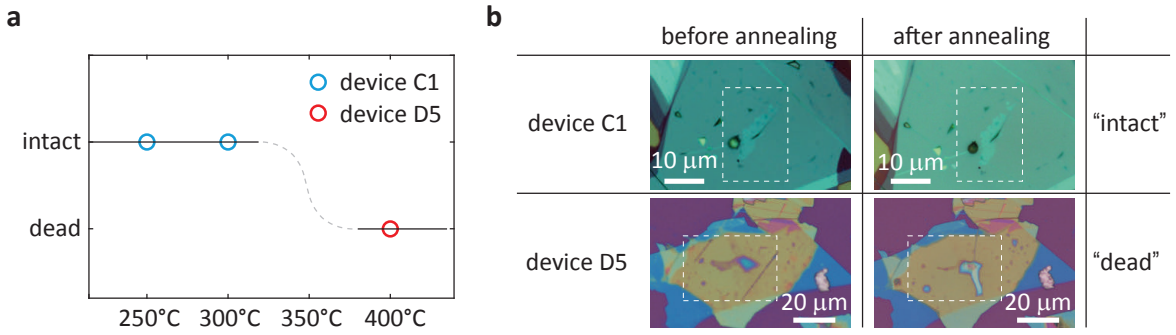

Figure 4.8: **Annealing of encapsulated CrI_3 devices. a** Two different few-layer CrI_3 devices (blue: C1, red: D5) were annealed for 1h at different temperatures. The exact transition from annealing at 300°C, where the samples stay intact, to 400°C, where the samples change has not been determined and is indicated with a gray dotted line. **b** Optical microscope images of devices C1 and D5, before and after annealing.

if upon annealing – and thus releasing strain – the encapsulated CrI_3 devices start to arrange in the ferromagnetically coupled structure (rhombohedral phase) at low temperatures.

We performed a series of test-anneals on two CrI_3 samples to determine a suitable annealing temperature. The flakes were annealed in a high vacuum ($\sim 6 \times 10^{-7}$ mbar) annealing oven for one hour at temperatures between 200°C and 500°C. A minimum of 200°C was chosen, since the material should be robust at this temperature as it was heated up to similar temperatures during the fabrication process. The maximum was set to 500°C in order not to melt the material.

Figure 4.8 summarizes the results from the annealing tests. The CrI_3 flakes survive an annealing and stay intact at 300°C. We define *"intact"* by the criterion that no obvious change in shape and structure of the flake occurred (as visible via the magnification of an optical microscope). An example of a device, which stayed *"intact"* is shown in Fig. 4.8b, upper row. On the other hand we consider a device to be *"dead"* once the shape of the flake altered simnifically during the annealing process, as shown in Fig. 4.8b, lower row.

In future experiments it would be interesting to test the hypothesis of controlling magnetism in CrI_3 with thermal annealing. Therefore, a CrI_3 device with an even number of layers (i.e. a bi-layer) would be measured in a Raman microscope at low temperatures, annealed at 300°C and afterwards measured again with Raman at low temperatures. This would already give a first hint on whether or not a structural change in the material occurred due to annealing. Afterwards, NV scanning probe magnetometry at cryogenic temperatures can be used to verify if the initially non-magnetic sample changed to a magnetic state by structural modifications due to thermal annealing.

4.3 Magnetization Reversal

The study of domain formation in vdW materials is important for the understanding of magnetism in two dimensions. Fudamental material properties, such as the strength of exchange interaction, can be determined from domain characterization [38]. In this section, we investigate magnetization reversal in atomically thin CrI_3. To that end, we determine the magnetic field required to reverse the magnetization of an initially fully polarized CrI_3 flake. When discussing magnetization reversal it is important to distinguish between two cases: the coherent reversal of the spin polarization, as described by the Stoner-Wohlfarth model, and the reversal via domain propagation [8]. In the first case, an external magnetic field, which is defined as the *coercive field* B_c, is applied to the sample and the magnetization changes its sign instantaneously throughout the entire flake. In the second case, a domain starts to nucleate in the device and changes the spin polarization step by step until the entire flake reverses its magnetization. The magnetic field needed to induce a domain is defined as the *nucleation field* B_{nuc}.

In this section we will first discuss how a domain was induced in a tri-layer CrI_3 flake and give an upper and lower bound on the required nucleation field B_{nuc} (Sect. 4.3.1). Following this, the determination of the coercive field B_c in a monolayer CrI_3 is described in Sect. 4.3.2.

4.3.1 Inducing a Domain in CrI_3

During an initial attempt of measuring the coercive field B_c in tri-layer CrI_3 (sample $D_{2,3}$) a domain nucleated in the flake. Therefore, our measurement of B_c turned into the determination of the nucleation field B_{nuc} instead.

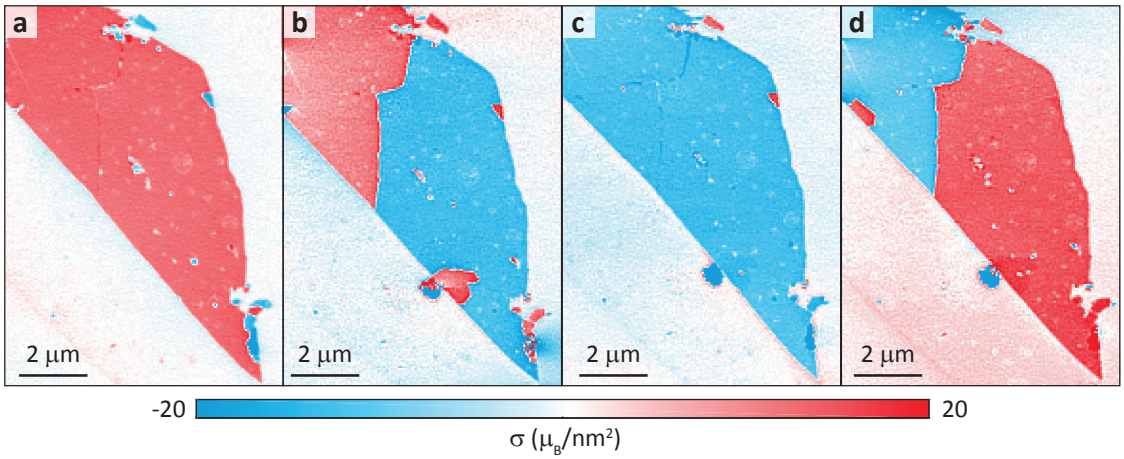

Figure 4.9: **Magnetic hysteresis cycle of a domain in tri-layer CrI_3.** **a** Positively magnetized tri-layer flake imaged in an external field of $B_{Bias\text{-}NV}$=172.5 mT. **b** First a maximal positive field in z-direction (B_z=495 mT) was applied and subsequently we induced the domain. For good ODMR contrast a field of $B_{Bias\text{-}NV}$=−172 mT was applied for imaging the domain. **c** Negatively magnetized tri-layer sample imaged at $B_{Bias\text{-}NV}$=−172 mT after a initializing the magnetic moments in B_z=−495 mT. **d** First, a field of B_z=−495 mT was applied to align the spins along the -z direction. Afterwards a domain was induced and later on imaged at $B_{Bias\text{-}NV}$=172.5 mT.

Figure 4.9 shows the cycle of inducing a domain in an initially positively (Fig. 4.9a,b) polarized and initially negatively polarized (Fig.4.9c,d) flake. During each measurement we applied a field $B_{\text{Bias-NV}}$ along the NV-axis. For the study of magnetization reversal in CrI_3, however, only the transverse component B_z of the applied field is relevant since the magnetic moments of the material are aligned along the z-axis (c.f. Sect. 2.1). The domain observed in Fig. 4.9b,d consistently nucleated at $B_z = \pm 111\,\text{mT}$ and was typically stable up to $B_z \sim 137\,\text{mT}$ (the latter value was only determined in a positive field). From this we conclude that the domain was not affected by a change in field $B_z < (137\,\text{mT} - 111\,\text{mT}) = 26\,\text{mT}$ along the z-axis. Therefore, we could apply the nucleation field $B_{\text{nuc}} = 111\,\text{mT}$ to create the domain but image the flake at a slightly smaller field $B_z = \pm 91\,\text{mT}$, which corresponds to $B_{\text{Bias-NV}} = 172\,\text{mT}$ along the NV-axis and yielded the best ODMR contrast.

Repeating the measurements consistently induced the same domain as depicted in Fig. 4.9, and the nucleation always started from the right lower corner of the device. We speculate that the CrI_3 flake had an energetically favorable region for the domain to nucleate there due to impurities, which could have locally lowered the anisotropy in the sample. However, it was not possible to capture the domain in a small corner of the flake – it would only appear at once in the middle of the flake. From this we conclude that a very strong pinning site was present in the sample, but it is not known what caused it. As visible in Fig. 4.9a, small inhomogeneities in the sample occur within the entire flake, especially along the domain pinning site. The nature of these impurities is yet to be investigated.

4.3.2 Coercive Field B_c for Monolayer CrI_3

In this section we describe the measurement procedure for determining the coercive field B_c required to coherently flip the magnetization of monolayer CrI_3. First, a negative field of $B_{\text{Bias-NV}} = -450\,\text{mT}$ ($-238\,\text{mT}$ in z-direction) was applied to align all spins anti-parallel to the $+z$-direction. Subsequently, we increased the external field in multiple steps and determined the magnetic orientation of the flake with line scans over the sample edge. Again, we point out the the external field was always applied along the NV-axis ($B_{\text{Bias-NV}}$) but the relevant parameter for studying the coercive field in CrI_3 is the transverse component of the field: B_z.

Figure 4.10 summarizes the individual steps for determining the coercive field B_c in a monolayer CrI_3 flake. In Fig. 4.10a the stray field from a negatively polarized single CrI_3 layer is shown together with the diamond scanning probe. The NV orientation is depicted as a gray arrow, i.e. the NV points away from the sample edge. The line scans were always taken perpendicularly to the sample edge as illustrated with the black arrow in Fig. 4.10b. Analytical fits to the line cuts yielded values for the magnetization σ. It is important to note that the noisy data of the linecuts in in Fig. 4.10c-f (due to the inhomogeneities in the sample and the coarse spacing between the data points) could not be fitted nicely. Therefore, the two NV orientation angles ϕ_{NV} and θ_{NV} were fixed during the fitting routine (the parameters obtained from reverse propagation on sample D_1 were chosen). We thus emphasize that here the fits in Fig.4.10 are rather a guideline to the eye than a reliable, quantitative source for determining σ.

After the magnetic moments were initialized in a negative field $B_z = -238\,\text{mT}$ in a first step ($B_{\text{Bias-NV}} = -450\,\text{mT}$), the field was increased to $B_z = -92\,\text{mT}$ ($B_{\text{Bias-NV}} = -172.5\,\text{mT}$) in a second step. The corresponding line cut is plotted in Fig. 4.10c and shows a negative field with a

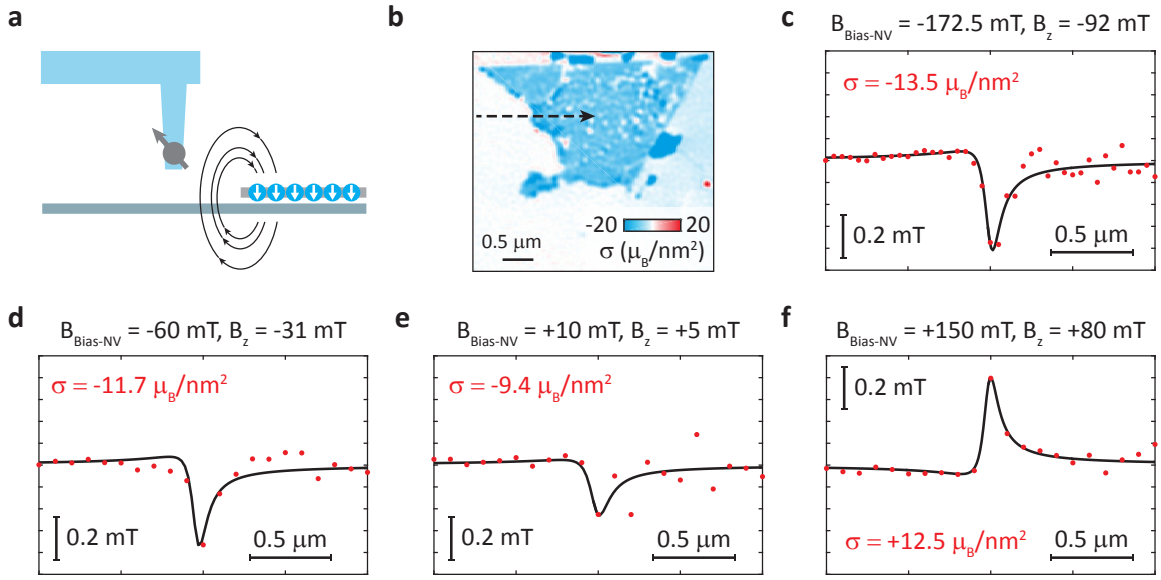

Figure 4.10: **Finding an upper bound for the coercive field B_c of monolayer CrI_3.** **a** Diamond scanning probe (blue) including the embedded NV center (gray, arrow denotes the NV orientation relative to the sample) above a negatively magnetized monolayer CrI_3. **b** Monolayer flake (image from Fig.4.2b) with a black arrow denoting the position of the line cuts taken in **c** to **f**. **c -e**: Line cuts at B_z=−92 mT, B_z=−31 mT and B_z=5 mT correspond to a negatively polarized flake. **f** Magnetization reversed in a field of B_z=80 mT, which sets an upper bound to the coercive field B_c.

fitted value of σ= -13.5 ± 1.4μ_B/nm^2. Subsequently, the line cut was repeated at B_z=−31 mT ($B_{\text{Bias-NV}}$=−60 mT), as shown in Fig. 4.10d. Again we observe a negative field, and the fit yields σ= -11.7 ± 2.1μ_B/nm^2. Applying a positive field B_z=5 mT ($B_{\text{Bias-NV}}$=10 mT), as illustrated with the line cut in Fig. 4.10e, did not flip the magnetization (σ= -9.4 ± 3.9μ_B/nm^2) of the flake. Only in a field B_z=80 mT ($B_{\text{Bias-NV}}$=150 mT), the magnetization changed its sign as shown in Fig. 4.10f, σ= +12.5 ± 1.7μ_B/nm^2.

After the last line scan we verified with a two-dimensional ODMR map that the magnetization was indeed reversed. The corresponding magnetic field map and the magnetization image are shown in Fig. 4.11. From our measurement an upper bound for the coercive field in z-direction B_c $\leqslant$ 80 mT can be stated, which is below to the values of B_c around 130 mT reported in [3, 39]. Unfortunately, it was not possible to determine B_c more precisely, i.e. with a lower bound since during these measurements the NV ODMR contrast was too small (<1%) at fields between 5 mT$\leqslant$ B_z $\leqslant$80 mT, respectively for the corresponding fields along the NV-axis 10 mT$\leqslant$ $B_{\text{Bias-NV}}$ $\leqslant$150 mT.

Surprisingly, the magnetization map in Fig.4.11b looks different compared to previous measurements: in the middle of the monolayer flake the field and the magnetization vanish, which was not observed before (c.f. Fig.4.2). We assume that the bubble above the monolayer was damaged by the diamond tip during a scan, which could have also destroyed the CrI_3 layer underneath. Subsequent AFM images (performed in a Bruker Dimension 3100 AFM, AFM tip diameter ∼10 nm) of the device corroborate this hypothesis. Figure 4.12a shows the topography of the monolayer part. The bright spot corresponds to the bubble over the flake. By comparing its shape to the original bubble (c.f. Fig. 3.3) it is evident that a change

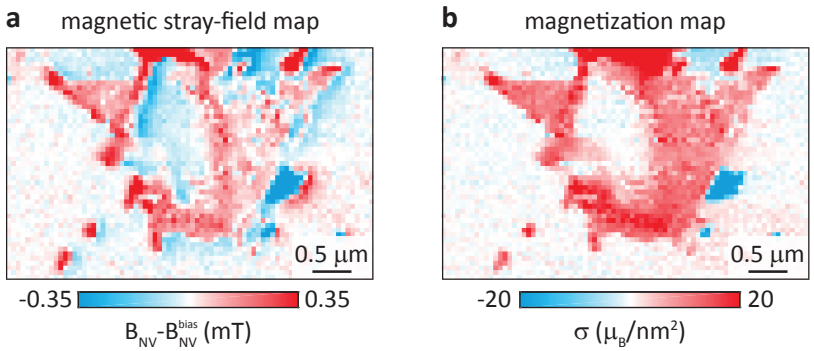

Figure 4.11: **Monolayer CrI_3 after magnetization reversal. a** Magnetic stray field arising from the monolayer flake measured at $B_{Bias\text{-}NV}$=170 mT. **b** Magnetization map revealing that part of the material in the center of the flake has vanished.

occurred. A line cut showing the height profile (red lines in Fig. 4.12a and b) confirms that a crater was formed in the middle of the monolayer flake: Figure 4.12b plots the height profile of the line cut. The first points of the line cut belong to the surface of the encapsulation material (graphene) only. Moving roughly 0.8 µm towards the right along the line cut, a first pump appears. Afterwards, the topography reaches the zero-level again, i.e. the level of the encapsulation, which agrees with the assumption that the middle part of the monolayer CrI_3 has vanished and a crater was formed. Furthermore, we measure a difference between the level of encapsulation and the level of bi-layer CrI_3 at the end of the line cut (black dotted line in Fig.4.12b): The difference in height amounts to roughly ∼1.4 nm, as expected for bi-layer CrI_3 (2 x monolayer-height $= 2 \cdot 0.7\,\text{nm} = 1.4\,\text{nm}$).

It is noteworthy that damaging the bubble in Fig. 4.11b did not affect the magnetization

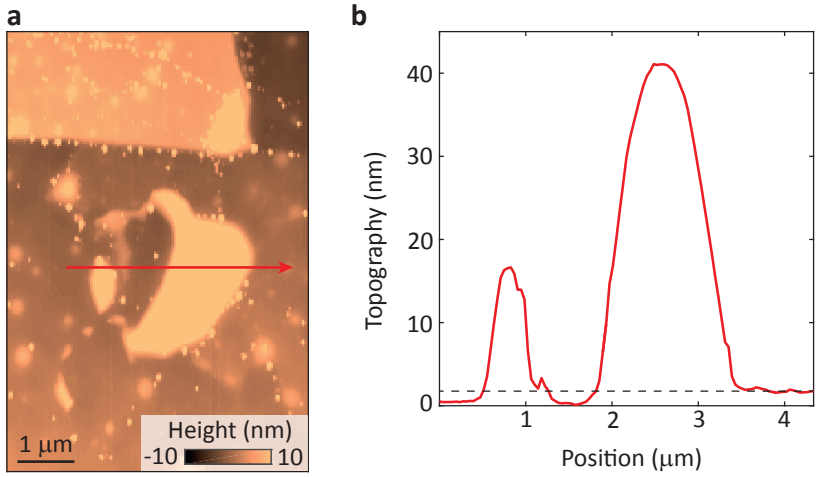

Figure 4.12: **Damaged bubble above monolayer CrI_3. a** Atomic force microscope (AMF) image (taken in a Bruker Dimension 3100 AFM) of the monolayer region. The bubble (bright spot in the center of the image) was punctured probably by the diamond tip. **b** Height profile along the line cut (red arrow in **a**) starting at the level of encapsulation and ending on the bi-layer region. Height difference from bi-layer to encapsulation ∼1.4 nm as indicated by the black dotted line.

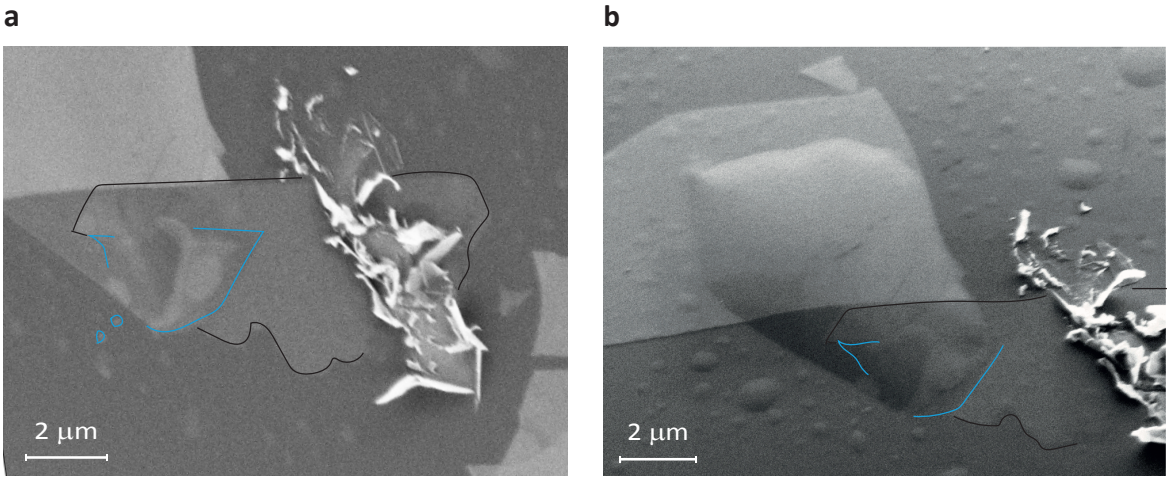

Figure 4.13: **Scanning electron beam (SEM) images of sample D_1. a** Black outline denotes the bi-layer flake and the blue outline highlights the monolayer area. The diamond tip crashed into the sample surface and cut open parts of the bilayer flake. **b** Tilted view of sample D_1.

of the adjacent bi-layer. Similarly, poking a hole into nine-layer CrI_3 did not change the interlayer coupling in the adjacent five-layer part (c.f. Sect.4.2). This suggests that a structural modification (and possibly a change in magnetic coupling) only has a local impact on the CrI_3 layer without affecting any adjacent layers. Possibly, the mono- and bi-layer part of the sample were not connected as it was also the case for the five- and the nine-layers parts in sample $D_{5,9}$.

Unfortunately, any further investigations on structural modifications were interrupted as during an overnight scan the diamond tip unexpectedly crashed into the sample surface and the pillar containing the NV center broke off. Subsequent scanning electron beam (SEM) images in Fig. 4.13 show that the diamond tip scratched open a trench in the bi-layer region. For clarification the bilayer part is outlined with a black line and the monolayer part is highlighted with a blue line. Surprisingly, the monolayer parts around the crater are still visible in image Fig. 4.13, which means that they did not degrade in air during the transportation from the measurement setup to the SEM. Either the crater sealed all the transitions between air and monolayer CrI_3 or the sample was more robust to air exposure than expected. The shape of the bubble above the monolayer flake from Fig. 4.13a (blue lines indicate the monolayer part and the bubble on top has a light gray color) is similar to the shape observed in AFM, c.f. Fig. 4.12. Furthermore, a tilted view onto the sample, c.f. Fig. 4.13b, shows that the entire flake – including the altered bubble – was possibly placed on top of another, larger bubble.

SEM images in Fig. 4.14 confirm that the NV tip broke off at its end while crashing into the sample. In the center of the cantilever (Fig. 4.14a, upside down view of the cantilever) the broken pillar is visible. A close-up view of the pillar in Fig. 4.14b shows that the tip broke off. Probably, the diamond pillar got caught somewhere on the flake surface during the scan and broke off as the cantilever moved further.

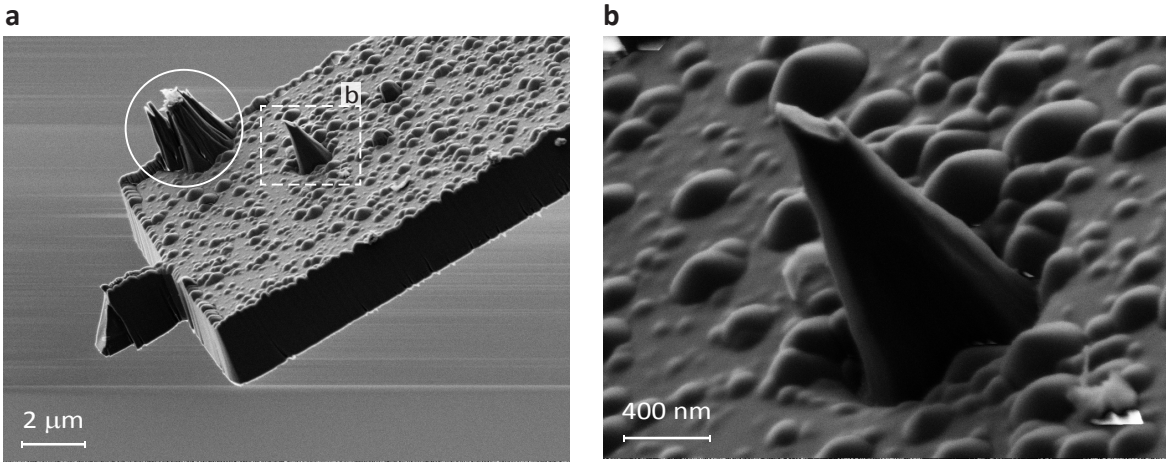

Figure 4.14: **SEM image of the cantilever after the pillar broke off.** **a** Upside-down view of the diamond cantilever with the pillar (framed with a white dashed box) in its center. A second arrangement of sharp spikes (indicated by white circle, residuals from the fabrication process) is present. **b** Diamond pillar with broken tip.

In summary, in this section we discussed our measurements showing magnetization reversal in tri-layer CrI_3 via inducing a domain in the center of the flake. The required nucleation field was determined to be $B_{nuc}=\pm 111\,mT$. For monolayer CrI_3 it was possible to set an upper bound to the coercive field $B_c \leqslant 80\,mT$.

5 Conclusion and Outlook

In this Thesis we report on our study of magnetism in the two-dimensional vdW magnet CrI_3 using single NV quantum sensors in diamond for quantitative magnetic imaging. A scanning probe technique with NV centers embedded in a diamond pillar was employed to measure the stray field emerging from thin CrI_3 flakes at cryogenic temperatures. Using a reverse propagation method for ferromagnetic thin films we could determine the magnetization of few-layer CrI_3 down to the monolayer limit.

- We consistently find an average magnetization of $\sim 16\ \mu_B/\mathrm{nm}^2$ for an odd number of CrI_3 layers, which is comparable to the theoretical value of one fully polarized layer of $14.7\ \mu_B/\mathrm{nm}^2$. Furthermore, we verified that bi-layer CrI_3 shows no net magnetization. We conclude from our measurements that antiferromagnetic interlayer exchange coupling is present in CrI_3 at low-temperatures and therefore we can confirm the even-odd effect.

- We demonstrated a switching of the magnetic order in CrI_3 from antiferromagnetic to ferromagnetic interlayer exchange coupling by a structural modification of the crystal (via a puncture of the material). This implies a correlation between crystal structure and magnetic order in CrI_3. Such a relation could also explain the observation of domains with a magnetization in even or odd integers of the monolayer magnetization σ_{mono}: Local variations of the interlayer exchange coupling due to changes in the crystal structure could lead to differently coupled domain regions in CrI_3.

- Low-temperature Raman spectroscopy was used to shed light onto different stacking orders in CrI_3. Additionally, we were able to record room-temperature Raman signals from few-layer and bi-layer CrI_3 devices. Our measurements show that acquiring a Raman spectrum on thin ($n_{\mathrm{layers}} < 10$) encapsulated CrI_3 flakes is challenging due to strong background Raman signals at low frequencies, which probably result from low-frequency modes of the graphene ($n_{\mathrm{layers}} > 3$) encapsulation.

- Finally, magnetization reversal in CrI_3 was studied. First, we were able to induce a domain in tri-layer CrI_3 and determined the corresponding nucleation field to be $B_{\mathrm{nuc}} = \pm 111\,\mathrm{mT}$. Second, for monolayer CrI_3 we were able to determine an upper bound on the coercive field required to coherently flip the magnetization as $B_c \leqslant 80\,\mathrm{mT}$.

Our studies on CrI_3 demonstrate the potential of NV-based quantum sensing as a useful tool for the study of vdW materials. Such experiments could help develop two-dimensional magnetic materials into novel, atomic-scale platforms for spintronics and magnonics applications.

In the future, our NV scanning probe could be used to measure gated CrI_3 devices. This would permit to verify wether recently observed changes in bi-layer CrI_3 by means of electrostatic doping or applied electric fields are indeed based on a change in the spin configuration from antiferromagnetic to ferromagnetic, or simply result from broken inversion symmetry [1, 39]. Furthermore, we would like to establish Raman spectroscopy on very thin CrI_3 layers as a useful characterization tool for stacking order in the vdW magnet. In general, further investigations on the correlation of interlayer exchange coupling and the crystal structure of CrI_3 are required. In this context we would like to investigate with thermal annealing if strain from the encapsulation affects the coupling nature (antiferromagnetic or ferromagnetic) in CrI_3 devices. In the long term it would be interesting to study magnonic excitations in CrI_3 [40]. By inducing a domain in the material, the anisotropy is locally zero (at the domain itself), potentially making it possible to excite low-frequency spin waves in CrI_3.

Bibliography

[1] B. Huang, G. Clark, D. R. Klein, D. MacNeill, E. Navarro-Moratalla, K. L. Seyler, N. Wilson, M. A. McGuire, D. H. Cobden, D. Xiao, W. Yao, P. Jarillo-Herrero, and X. Xu, "Electrical control of 2d magnetism in bilayer CrI_3," *Nature Nanotechnology*, vol. 13, no. 7, pp. 544–548, 2018. [Online]. Available: https://doi.org/10.1038/s41565-018-0121-3

[2] D. R. Klein, D. MacNeill, J. L. Lado, D. Soriano, E. Navarro-Moratalla, K. Watanabe, T. Taniguchi, S. Manni, P. Canfield, J. Fernández-Rossier, and P. Jarillo-Herrero, "Probing magnetism in 2d van der Waals crystalline insulators via electron tunneling," *Science*, vol. 360, no. 6394, pp. 1218–1222, 2018. [Online]. Available: http://science.sciencemag.org/content/360/6394/1218

[3] B. Huang, G. Clark, E. Navarro-Moratalla, D. R. Klein, R. Cheng, K. L. Seyler, D. Zhong, E. Schmidgall, M. A. McGuire, D. H. Cobden, W. Yao, D. Xiao, P. Jarillo-Herrero, and X. Xu, "Layer-dependent ferromagnetism in a van der Waals crystal down to the monolayer limit," *Nature*, vol. 546, p. 270, Jun 2017. [Online]. Available: https://doi.org/10.1038/nature22391

[4] L. Thiel, Z. Wang, M. A. Tschudin, D. Rohner, I. Gutiérrez-Lezama, N. Ubrig, M. Gibertini, E. Giannini, A. F. Morpurgo, and P. Maletinsky, "Probing magnetism in 2D materials at the nanoscale with single spin microscopy," *Under review*, 2018.

[5] J. M. Taylor, P. Cappellaro, L. Childress, L. Jiang, D. Budker, P. R. Hemmer, A. Yacoby, R. Walsworth, and M. D. Lukin, "High-sensitivity diamond magnetometer with nanoscale resolution," *Nature Physics*, vol. 4, p. 810, 2008. [Online]. Available: https://doi.org/10.1038/nphys1075

[6] J. R. Maze, P. L. Stanwix, J. S. Hodges, S. Hong, J. M. Taylor, P. Cappellaro, L. Jiang, M. V. G. Dutt, E. Togan, A. S. Zibrov, A. Yacoby, R. L. Walsworth, and M. D. Lukin, "Nanoscale magnetic sensing with an individual electronic spin in diamond," *Nature*, vol. 455, p. 644, 2008. [Online]. Available: https://doi.org/10.1038/nature07279

[7] M. A. McGuire, H. Dixit, V. R. Cooper, and B. C. Sales, "Coupling of crystal structure and magnetism in the layered, ferromagnetic insulator CrI_3," *Chemistry of Materials*, vol. 27, no. 2, pp. 612–620, 2015. [Online]. Available: https://doi.org/10.1021/cm504242t

[8] A. Aharoni, "An introduction to the theory of ferromagnetism," *Oxford University Press*, 2000.

[9] R. Gross and M. Achim, "Festkörperphysik," *Oldenbourg Verlag München*, 2014.

[10] "CrI_3 crystal structure," *Springer-Verlag Berlin Heidelberg & Material Phases Data System (MPDS), Switzerland & National Institute for Materials Science (NIMS), Japan*, accessed 2019-01-14. [Online]. Available: https://materials.springer.com/isp/crystallographic/docs/sd_0308014

[11] A. K. Geim and I. V. Grigorieva, "Van der Waals heterostructures," *Nature*, vol. 499, p. 419, 2013. [Online]. Available: https://doi.org/10.1038/nature12385

[12] B. Shabbir, M. Nadeem, Z. Dai, M. S. Fuhrer, Q.-K. Xue, X. Wang, and Q. Bao, "Long range intrinsic ferromagnetism in two dimensional materials and dissipationless future technologies," *Applied Physics Reviews*, vol. 5, no. 4, p. 041105, 2018. [Online]. Available: https://doi.org/10.1063/1.5040694

[13] J. L. Lado and J. Fernández-Rossier, "On the origin of magnetic anisotropy in two dimensional CrI_3," *2D Materials*, vol. 4, no. 3, p. 035002, 2017. [Online]. Available: http://stacks.iop.org/2053-1583/4/i=3/a=035002

[14] N. D. Mermin and H. Wagner, "Absence of ferromagnetism or antiferromagnetism in one- or two-dimensional isotropic heisenberg models," *Phys. Rev. Lett.*, vol. 17, pp. 1133–1136, 1966. [Online]. Available: https://link.aps.org/doi/10.1103/PhysRevLett.17.1133

[15] S. Feldkemper and W. Weber, "Generalized calculation of magnetic coupling constants for mott-hubbard insulators: Application to ferromagnetic Cr compounds," *Phys. Rev. B*, vol. 57, pp. 7755–7766, 1998. [Online]. Available: https://link.aps.org/doi/10.1103/PhysRevB.57.7755

[16] L. Chen, J.-H. Chung, B. Gao, T. Chen, M. B. Stone, A. I. Kolesnikov, Q. Huang, and P. Dai, "Topological spin excitations in honeycomb ferromagnet CrI_3," *Phys. Rev. X*, vol. 8, no. 4, p. 041028, 2018. [Online]. Available: https://link.aps.org/doi/10.1103/PhysRevX.8.041028

[17] D. Soriano, C. Cardoso, and J. Fernández-Rossier, "Interplay between interlayer exchange and stacking in CrI_3 bilayers," *arXiv:1807.00357*, 2018. [Online]. Available: https://arxiv.org/abs/1807.00357

[18] N. Sivadas, S. Okamoto, and D. Xiao, "Gate-controllable magneto-optic kerr effect in layered collinear antiferromagnets," *Phys. Rev. Lett.*, vol. 117, no. 26, p. 267203, 2016. [Online]. Available: https://link.aps.org/doi/10.1103/PhysRevLett.117.267203

[19] P. Maletinsky, S. Hong, M. S. Grinolds, B. Hausmann, M. D. Lukin, R. L. Walsworth, M. Loncar, and A. Yacoby, "A robust scanning diamond sensor for nanoscale imaging with single nitrogen-vacancy centres," *Nature Nanotechnology*, vol. 7, p. 320, 2012. [Online]. Available: http://dx.doi.org/10.1038/nnano.2012.50

[20] F. Casola, T. van der Sar, and A. Yacoby, "Probing condensed matter physics with magnetometry based on nitrogen-vacancy centres in diamond," *Nature Reviews Materials*, vol. 3, p. 17088, 2018. [Online]. Available: http://dx.doi.org/10.1038/natrevmats.2017.88

[21] L. M. Pham, "Magnetic field sensing with nitrogen-vacancy color centers in diamond," *Harvard University*, 2013. [Online]. Available: http://walsworth.physics.harvard.edu/publications/2013_Pham_HUPhDThesis.pdf

[22] L. Rondin, J.-P. Tetienne, T. Hingant, J.-F. Roch, P. Maletinsky, and V. Jacques, "Magnetometry with nitrogen-vacancy defects in diamond," *Reports on Progress in Physics*, vol. 77, no. 5, p. 056503, 2014. [Online]. Available: http://stacks.iop.org/0034-4885/77/i=5/a=056503

[23] N. B. Manson, J. P. Harrison, and M. J. Sellars, "Nitrogen-vacancy center in diamond: Model of the electronic structure and associated dynamics," *Phys. Rev. B*, vol. 74, p. 104303, 2006. [Online]. Available: https://link.aps.org/doi/10.1103/PhysRevB.74.104303

[24] R. Schirhagl, K. Chang, M. Loretz, and C. L. Degen, "Nitrogen-vacancy centers in diamond: Nanoscale sensors for physics and biology," *Annu. Rev. Phys. Chem.*, vol. 65, no. 1, pp. 83–105, 2014. [Online]. Available: https://doi.org/10.1146/annurev-physchem-040513-103659

[25] D. Riedel, I. Söllner, B. J. Shields, S. Starosielec, P. Appel, E. Neu, P. Maletinsky, and R. J. Warburton, "Deterministic enhancement of coherent photon generation from a nitrogen-vacancy center in ultrapure diamond," *Phys. Rev. X*, vol. 7, p. 031040, 2017. [Online]. Available: https://link.aps.org/doi/10.1103/PhysRevX.7.031040

[26] M. W. Doherty, N. B. Manson, P. Delaney, F. Jelezko, J. Wrachtrup, and L. C. Hollenberg, "The nitrogen-vacancy colour centre in diamond," *Physics Reports*, vol. 528, no. 1, pp. 1–45, 2013. [Online]. Available: http://www.sciencedirect.com/science/article/pii/S0370157313000562

[27] V. M. Acosta, L. S. Bouchard, D. Budker, R. Folman, T. Lenz, P. Maletinsky, D. Rohner, Y. Schlussel, and L. Thiel, "Color centers in diamond as novel probes of superconductivity," *arXiv:1808.03282*, 2018. [Online]. Available: https://arxiv.org/abs/1808.03282

[28] E. Meyer, H. J. Hug, and R. Bennewitz, "Scanning probe microscopy," *Springer-Verlag Berlin Heidelberg*, 2004. [Online]. Available: https://link.springer.com/book/10.1007/978-3-662-09801-1

[29] P. Appel, B. J. Shields, T. Kosub, R. Hübner, J. Faßbender, D. Makarov, and P. Maletinsky, "Nanomagnetism of magnetoelectric granular thin-film antiferromagnets," *arXiv:1806.02572*, 2018. [Online]. Available: https://arxiv.org/abs/1806.02572

[30] T. Hingant, J.-P. Tetienne, L. J. Martínez, K. Garcia, D. Ravelosona, J.-F. Roch, and V. Jacques, "Measuring the magnetic moment density in patterned ultrathin ferromagnets with submicrometer resolution," *Phys. Rev. Applied*, vol. 4, p. 014003, Jul 2015. [Online]. Available: https://link.aps.org/doi/10.1103/PhysRevApplied.4.014003

[31] J.-P. Tetienne, T. Hingant, L. Martínez, S. Rohart, A. Thiaville, L. H. Diez, K. Garcia, J.-P. Adam, J.-V. Kim, J.-F. Roch, I. Miron, G. Gaudin, L. Vila, B. Ocker, D. Ravelosona, and V. Jacques, "The nature of domain walls in ultrathin ferromagnets

revealed by scanning nanomagnetometry," *Nature Communications*, vol. 6, p. 6733, Apr. 2015. [Online]. Available: https://doi.org/10.1038/ncomms7733

[32] L. Thiel, D. Rohner, M. Ganzhorn, P. Appel, E. Neu, B. Müller, R. Kleiner, D. Koelle, and P. Maletinsky, "Quantitative nanoscale vortex imaging using a cryogenic quantum magnetometer," *Nature Nanotechnology*, vol. 11, p. 677, 2016. [Online]. Available: https://doi.org/10.1038/nnano.2016.63

[33] P. Appel, E. Neu, M. Ganzhorn, A. Barfuss, M. Batzer, M. Gratz, A. Tschöpe, and P. Maletinsky, "Fabrication of all diamond scanning probes for nanoscale magnetometry," *Review of Scientific Instruments*, vol. 87, no. 6, p. 063703, 2016. [Online]. Available: https://doi.org/10.1063/1.4952953

[34] S. Jiang, J. Shan, and K. F. Mak, "Electric-field switching of two-dimensional van der Waals magnets," *Nature Materials*, vol. 17, no. 5, pp. 406–410, May 2018. [Online]. Available: https://doi.org/10.1038/s41563-018-0040-6

[35] S. Djurdjic-Mijin, A. Šolajić, J. Pešić, M. Šćepanović, Y. Liu, A. Baum, C. Petrovic, N. Lazarević, and Z. V. Popović, "Lattice dynamics and phase transition in CrI_3 single crystals," *Phys. Rev. B*, vol. 98, p. 104307, Sep 2018. [Online]. Available: https://link.aps.org/doi/10.1103/PhysRevB.98.104307

[36] D. Shcherbakov, P. Stepanov, D. Weber, Y. Wang, J. Hu, Y. Zhu, K. Watanabe, T. Taniguchi, Z. Mao, W. Windl, J. Goldberger, M. Bockrath, and C. N. Lau, "Raman spectroscopy, photocatalytic degradation, and stabilization of atomically thin chromium tri-iodide," *Nano Letters*, vol. 18, no. 7, pp. 4214–4219, 2018, pMID: 29863369. [Online]. Available: https://doi.org/10.1021/acs.nanolett.8b01131

[37] J. Wu, H. Xu, W. Mu, L. Xie, X. Ling, J. Kong, M. S. Dresselhaus, and J. Zhang, "Observation of low-frequency combination and overtone raman modes in misoriented graphene," *The Journal of Physical Chemistry C*, vol. 118, no. 7, pp. 3636–3643, 2014. [Online]. Available: https://doi.org/10.1021/jp411573c

[38] S. Kim, P.-H. Jang, D.-H. Kim, M. Ishibashi, T. Taniguchi, T. Moriyama, K.-J. Kim, K.-J. Lee, and T. Ono, "Magnetic droplet nucleation with a homochiral néel domain wall," *Phys. Rev. B*, vol. 95, p. 220402, 2017. [Online]. Available: https://link.aps.org/doi/10.1103/PhysRevB.95.220402

[39] S. Jiang, L. Li, Z. Wang, K. F. Mak, and J. Shan, "Controlling magnetism in 2d CrI_3 by electrostatic doping," *Nature Nanotechnology*, vol. 13, no. 7, pp. 549–553, 2018. [Online]. Available: https://doi.org/10.1038/s41565-018-0135-x

[40] A. V. Chumak, V. Vasyuchka, A. Serga, and B. Hillebrands, "Magnon spintronics," *Nature Physics*, vol. 11, p. 453, 2015. [Online]. Available: https://doi.org/10.1038/nphys3347

[41] C. Gerry and P. Knight, "Introductory quantum optics," *Cambridge university press*, 2005.

A Correlation function $g^{(2)}(\tau)$

By measuring the correlation function $g^{(2)}(\tau)$ we verified that our employed NV center was indeed a single spin. As shown in Fig. A.1 below, the $g^{(2)}(\tau = 0)$ dip goes below 0.5, which is expected for a single quantum emitter [41].

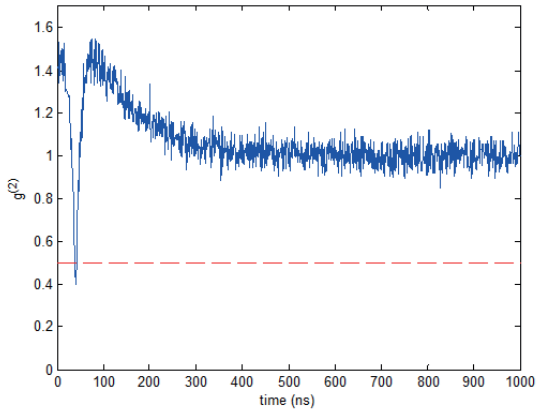

Figure A.1: $g^{(2)}(\tau)$ of a single NV center.

B Heating from Laser Irradiation and Microwave Power

This figure is based on the section "non-invasiveness of imaging method" in the supplementary of [4].

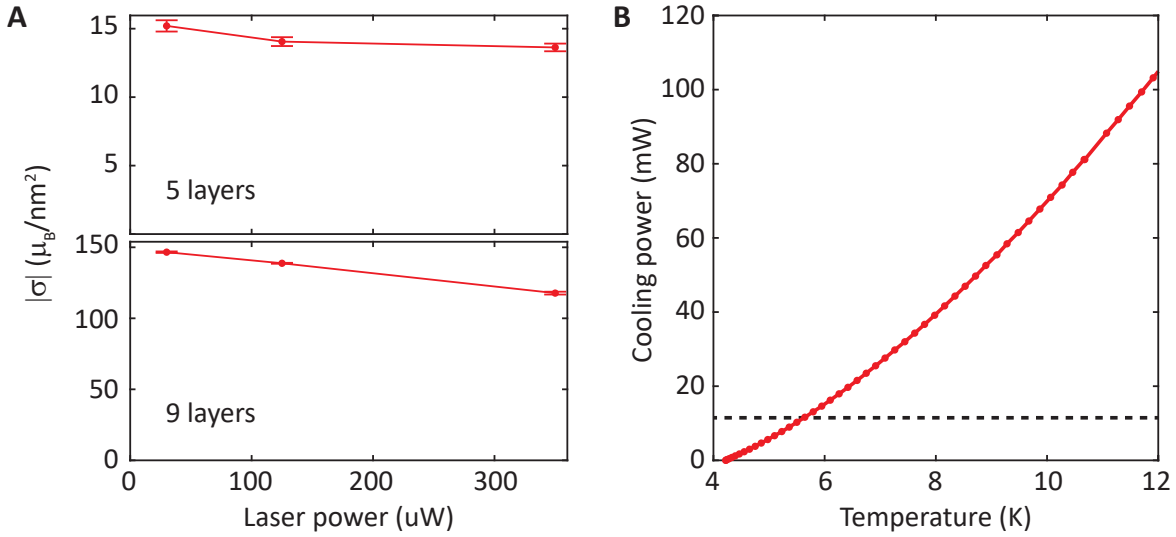

Figure B.1: **Impact of laser power and microwave heating.** **a** Influence of the 532 nm laser power on the magnetization σ. For laser powers above 100 µW the measured value of σ decreases compared to the results obtained at lower laser powers. Choosing a power $P_{laser} \sim 40$ µW for all measurements ensures that no significant back-action from the laser power was induced onto the samples. The magnetization σ was determined by analytical fits to line scans over the sample edges. The measurements on the nine-layer flake were performed after the puncture (hence a larger value of σ is observed compared to the five-layer data points). **b** The cooling power (red dotted line) of the He bath cryostat is plotted with respect to the temperature. The black dashed line represents the estimated microwave power arriving at the cryostat. From the plot we conclude that heating due to microwave power leads to a measurement temperature of ~ 7 K, which is far below the Curie temperature of monolayer CrI_3 ($T_c = 45$ K [3]). Therefore, we infer that heating from the microwave antenna did not influence the magnetization of the sample.

C ODMR Contrast

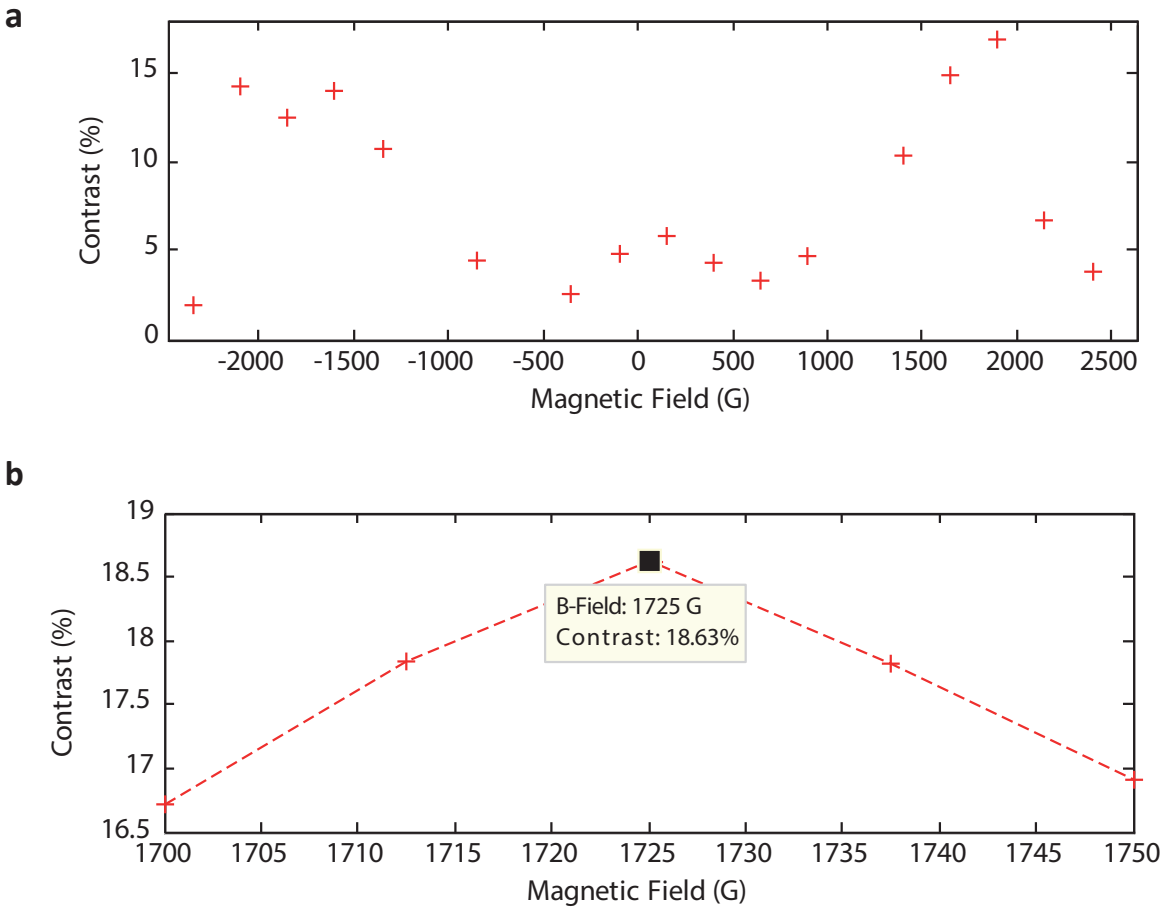

Figure C.1: **ODMR contrast measured as a function of applied external field along the NV-axis.** **a** Maximal contrast is observed for fields between $\pm 150\,\mathrm{mT}$ and $\pm 200\,\mathrm{mT}$. **b** A more detailed measurement shows that the maximal ODMR contrast of $\sim$ 18% is achieved in a external field of $\pm 172.5\,\mathrm{mT}$ along the NV-axis.

hBN Rorschach Flakes - special Appendix

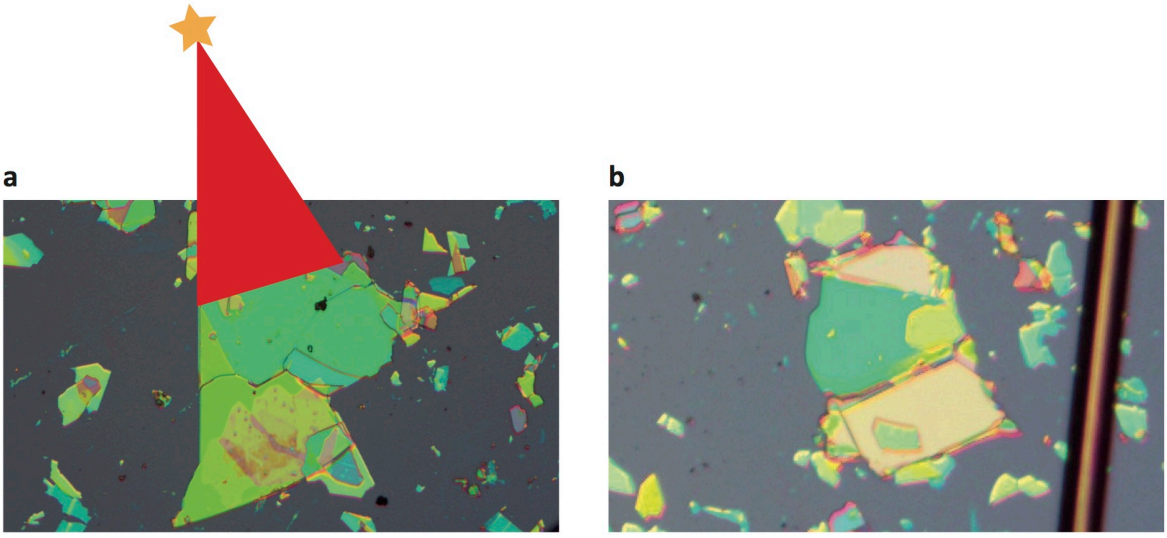

Optical microscope images of our two favorite hBN flakes. Personally, I see: **a** A dinosaur with a red hat. **b** *Ein Männchen im Schneegestöber*. Both creatures are ∼200 µm in size.

Universität Basel

Philosophisch-Naturwissenschaftliche Fakultät

Erklärung zur wissenschaftlichen Redlichkeit

(beinhaltet Erklärung zu Plagiat und Betrug)

Masterarbeit

Titel der Arbeit *(Druckschrift)*:

Investigating Magnetism in Two-Dimensional CrI3 Using Single Spin Nitrogen-Vacancy Centers in Diamond

Name, Vorname *(Druckschrift)*: Tschudin, Märta

Matrikelnummer: 13-060-926

Mit meiner Unterschrift erkläre ich, dass mir bei der Abfassung dieser Arbeit nur die darin angegebene Hilfe zuteil wurde und dass ich sie nur mit den in der Arbeit angegebenen Hilfsmitteln verfasst habe.

Ich habe sämtliche verwendeten Quellen erwähnt und gemäss anerkannten wissenschaftlichen Regeln zitiert.

Diese Erklärung wird ergänzt durch eine separat abgeschlossene Vereinbarung bezüglich der Veröffentlichung oder öffentlichen Zugänglichkeit dieser Arbeit.

☐ ja ■ nein

Ort, Datum: Basel, 31.1.2019

Unterschrift: M. Tschudin

Dieses Blatt ist in die Bachelor-, resp. Masterarbeit einzufügen.